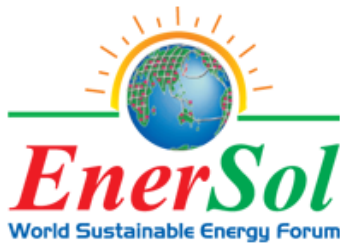




**SETCOR**  
Conferences & Events



**EnerSol World Sustainable Energy Forum**

**November, 26 - 28, 2014 - Tunis - Tunisia**

**World Sustainable Energy Forum  
EnerSol WSEF Tunisia 2014  
International Conference  
Proceeding**

[www.setcor.org/conferences/EnerSol-WSEF-2014](http://www.setcor.org/conferences/EnerSol-WSEF-2014)



# Silver nanoparticles contribution in optical response of MACE silicon nanowires structures

R. Benabderrahmane Zaghouani\*, S. Aouida, M. Rawefi, N. Bachtouli, B. Bessais.  
Photovoltaic Laboratory, Research and Technology Centre of Energy, Borj Cedria Science and Technology  
Park, BP N° 95, 2050 Hammam-Lif, Tunisia

\*Corresponding author. Dr. Rabia Benabderrahmane Zaghouani  
Tel.: +21654154428; fax: +21679325825  
E-mail address: [rabia.benabderrahmane@gmail.com](mailto:rabia.benabderrahmane@gmail.com)

## Abstract

This work focuses on optical characterization of silicon nanowires (SiNWs) used for photovoltaic applications. We report on the elaboration of SiNWs by Metal Assisted Chemical Etching technique (MACE) technique using silver (Ag) as metal catalyst. The obtained results show that the SiNWs optical properties are sensitive to their elaboration conditions specially the cleaning protocol. The comparison between samples with different cleaning protocol shows that, in the UV spectral region, SiNWs more contaminated with Ag nanoparticles (Ag-Nps) present a pronounced decrease of the reflectivity. This optical behavior was attributed to metallic nanoparticles persisting in the silicon nanowires structures presenting surface plasmon resonance energy in a vicinity of UV spectral region.

**Keywords:** SiNWs, MACE, Reflectivity, Silver nanoparticles, Surface Plasmon resonance.

## 1. Introduction

Silicon-based solar cells remain the main candidate in photovoltaic solar energy conversion. However, a large part of the solar cell conversion-efficiency limits are attributed to the optical losses in silicon material. That's why the scientific community is interested in developing concepts and technologies that enable reducing optical losses and thus enhance the solar cell efficiency. Conventionally, the surface reflectivity of silicon-based solar cells can be reduced by texturing the front side of the cell (Bachtouli et al.; 2012) and/or using appropriate antireflection (AR) coatings (Richards; 2004). During the last decade, important efforts have been dedicated to the use of SiNWs in photovoltaic applications. SiNWs deposited on the surface of silicon-based solar cells could act as an efficient antireflection layer. In this work, we have elaborated SiNWs with the Metal Assisted Chemical Etching technique using silver (Ag) as catalyst. We report on the effect of Ag-Nps on SiNWs optical behavior. Therefore, we study the sensitivity of SiNWs optical response with experimental conditions specially the cleaning protocol.

## 2. Experimental details

To elaborate silicon nanowires, the substrates used are boron-doped single crystalline silicon (100) with a resistivity of ~1-3 ohm.cm and a thickness of 300  $\mu\text{m}$ . Before SiNWs elaboration, silicon substrates were consecutively cleaned with acetone, ethanol and deionized water for 1 min in order to eliminate organic greases. Finally, the substrates are etched in 5% HF for 1min to eliminate native oxide. SiNWs were prepared by MACE method. The silicon substrates are immersed in a mixture of 10 ml HF (48%), 10 ml  $\text{AgNO}_3$  solution and 1 ml  $\text{H}_2\text{O}_2$  (30%) at room temperature for 40 min. Finally, the substrates are rinsed with water to stop the etching and with nitric acid ( $\text{HNO}_3$ ) to eliminate silver. The surface reflectivity of elaborated SiNWs was analyzed using a PerkinElmer Lambda 950 UV/VIS spectrometer. The morphological features of SiNWs were investigated using a JEOL JSM-5400 Scanning Electron Microscopy (SEM).

## 3. Results and discussion:

SiNWs are elaborated in  $\text{HF}/\text{AgNO}_3/\text{H}_2\text{O}_2$  solution. The first reaction consists on the capture of electrons by  $\text{Ag}^+$  ions from silicon surface leading to Ag-Nps deposition. The second reaction is dealing with silicon etching by the formation and dissolution of silicon oxide until the formation of quasi-regular SiNWs catalyzed by Ag-Nps (Figure 1). In order to investigate optical behavior of SiNWs, we have studied their reflectivity. We notice that the shape of reflectivity spectra is sensitive to experimental conditions specially the cleaning protocol. In Figure 2, we compare the total reflectivity of SiNWs cleaned in a concentrated  $\text{HNO}_3$  solution during 1min (sample A) and SiNWs cleaned in a diluted solution ( $\langle \text{HNO}_3:\text{H}_2\text{O} \rangle = \langle 1:1 \rangle$ ) during 1 min (sample B). Sample B, suspected

to be more contaminated with Ag-Nps, exhibits a pronounced decrease of the reflectivity in the UV spectral region compared to sample A. Ag-Nps may be responsible of the optical response observed. Ag-Nps are known to present a plasmonic effect and show surface plasmon resonance energy in the UV spectral region (Razaa et al.; 2013) when illuminated by light. This effect leads to an absorption increase and then to a reflectivity decrease.

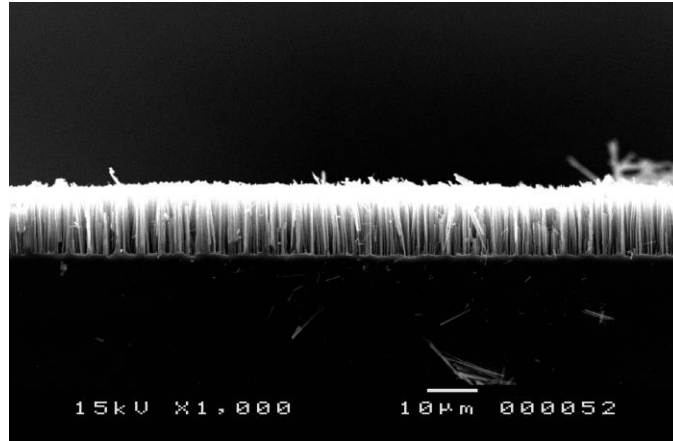


Figure.1:SEM cross-section view of SiNWs

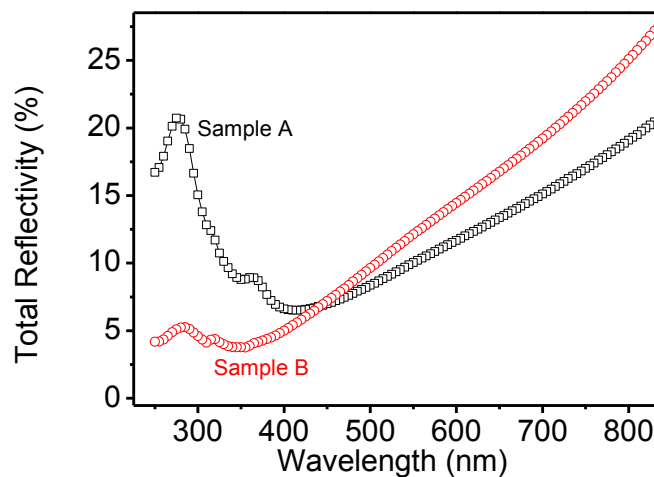


Figure 2 Reflectivity spectra of SiNWs: sample A and sample B rinsed in diluted and concentrated HNO<sub>3</sub>, respectively.

#### 4. Conclusions:

In this work, we have studied the effect of silver nanoparticles on the optical response of silicon nanowires. These nanoparticles are persisting in the structure even after cleaning with HNO<sub>3</sub> and are influencing the SiNWs reflectivity. They present a plasmonic effect when excited by light leading to a reflectivity decrease. This property seems to be interesting in order to verify the efficiency of the cleaning protocol.

#### References:

- Bachtouli, N., Aouida, S., HadjLaajimi, R., Boujmil, M.F., Bessais, B. (2012), Implications of alkaline solutions-induced etching on optical and minority carrier lifetime features of monocrystalline silicon, *Appl. Surf. Sci.*, 258, 8889-8894
- Richards, B.S. (2004), Comparison of TiO<sub>2</sub> and Other Dielectric Coatings for Buried-contact Solar Cells: a Review, *Prog. Photovolt: Res. Appl.*, 12, 253-281
- Razaa, S., Stengera, N., Kadkhodazadeh, S., Fischer, S. V., Kostasheva, N., Jauho, A.P., Burrows, A., Wubs, M., Mortensen, N. A. (2013), Blueshift of the surface plasmon resonance in silver nanoparticles: substrate effects, *Nanophotonics*, 2, 131-138.

# Extraction of High Purity Silica from Rice Husks Ash for Reduction to Silicon.

C. E. Ilochonwu<sup>1\*</sup>, I. U. Onyenanu<sup>2</sup>, P. N. Atanmo<sup>2</sup>

<sup>1</sup>Scientific Equipment Development Institute Enugu, Nigeria.

<sup>2</sup>Department of Mechanical Engineering, Anambra State University, Nigeria.

\*Corresponding author email: nwenchuks@yahoo.ca

## Abstract:

Rice Husks (RHs) biomass waste is very much abundant in developing countries like Nigeria. This work shows how pure silica was derived directly from rice husks ash for reduction to Silicon (Si). Si is the second most abundant element in the Earth's crust, but the processes to form Si materials is usually complex, costly and energy-intensive [4]. The silica in the ash undergoes structural transformations depending on the conditions (time, temperature etc.) of combustion. At 400°C to 700°C amorphous ash is formed and at temperatures greater than this crystalline ash is formed. A high purity silica was produced at 650°C after burning the rice husk RH for up to 7 hours. We determined the purity of the silica by dissolving the rice husk ash (RHA) with alkali solution to form sodium silicate solution of pH 11.0. This was added to hydrochloric acid of pH 1.5 which lowered the pH of the solution to 4.0 to form silica gels which was promoted by incubating it at room temperature for overnight. The silica gels produced were crushed inside the beakers, dispersed in deionized water of 100ml and the slurry was centrifuged at 5000rpm for 10min to remove soluble salt, the supernatant were discarded and the gels were subjected to washing and then dried at 80°C for 24 hours to obtain pure powder silica. The silica powder was characterized using XRD and EDX techniques. Silica yields from RHA was 99%. This study was done to reduce energy waste and environmental pollution in Nigeria as silicon is used to develop many materials.

Keywords: Rice Husk, silica, silicon, Rice Husk Ash.

## 1. Introduction

Globally, rice is a very important food crop. It is an ancient crop consumed as healthy and staple food by more than half of the world population. Rice is consumed by over 4.8 billion people in 176 countries and is the most important food crop for over 2.89 billion people in Asia, over 40 million people in Africa and over 150.3 million people in America with estimates based on FAO report of 1996. More than 90% of global production occurs in tropical and semi-tropical Asia [1]. Paddy, on an average, consists of about 72 percent of rice, 5-8 percent of bran, and 20-22 percent of husk [7]. Of all the plant residues, the ash of rice husk contains the highest proportion of

silica. It is estimated that every tonne of paddy produces about 0.20 tonnes of husk and every tonne of husk produces about 0.18 to 0.20 tonnes of ash, depending on the variety, climatic conditions and geographical location [7, 8].

Rice husk biomass waste is very much abundant in developing countries like Africa (Nigeria), South America, and Asia. This waste material can be found elsewhere and oftentimes we can see piles of rice husks at the back of the rice mill where they are stacked for disposal or some are thrown and burned on road sides to reduce its volume. This waste can be converted into fuel for domestic and wealth creation for other applications [9]. The treatment of rice husk as a resource for energy production is a departure from the perception that husks present disposal problems. The concept of generating energy from rice husk has great potential, particularly in those countries that are primarily depending on imported oil for their energy needs. Rice husks are one of the largest readily available but most under-utilized biomass resources, being an ideal fuel for electricity generation. The outer covering of commonly grown rice is comprised primarily of cellulose, lignin and silica [3].

Rice husk ash contains 87-97 percent of silica with small amount of alkalis and other trace elements [2]. Its absorbent and insulating properties are useful to many industrial applications [4]. Based on temperature range and duration of burning of the husk, crystalline and amorphous forms of silica are obtained [10, 11, 12, and 13]. The crystalline and amorphous forms of silica have different properties and it is important to produce ash with correct specifications for specific end use. Generally, the amorphous forms of silica are composed of silica tetrahedral arranged in a random three-dimensional network without regular lattice structures. Due to disordered arrangement, the structure is open with holes in the network where electrical neutrality is not satisfied and the specific surface area is also large. This helps to increase the reactivity, since large area is available for reaction to take place [14].

The technology of converting rice husk ash to amorphous silica is to dissolve it in acid/base

solutions to form precipitate or gels. This can be washed and dried to yield the intended product [5].

## 2. Materials and Methods

### 2.1 Preparation of the rice husk.

The Rice Husk (RH) used in this investigation was supplied by BSG HandCraft USA which they are using as needed to improve filter bed performance of wheat beer or other high protein mashes as normal usage up to 5%. The Rice Husk (RH) is not treated with anything before burning it to ashes. First the rice husk was sieved in a sieving system that collected the retained rice husks in the USA Standard Test Sieve No.8 of 2.38mm. The average size of the Rice Husk used is tabulated in table 1 below after measuring 30 pieces of Rice Husk.

Table 1. Average size of RH used.

Size	RH Dimension (mm)
Length	8.64
Width	2.09
Thickness	0.17

### 2.2 Thermal decomposition.

Based on literature data, you will get amorphous silica when you burn rice husks in the presence of oxygen for a long time at temperature below 700°C. So, burning temperature of 400°C, 450°C, 500°C, 550°C, 600°C and 650°C was chosen. The husks was burned inside a muffle furnace. For each burning 1000g of Rice husks was put inside a steel basket and placed inside the furnace under static air for 7 hours at heating rate of 7.01°C/min. See figure 1 below for the rice plant burnt to rice husk ash.



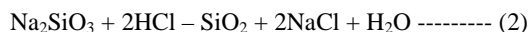
Figure 1: Rice plant, Rice Husk and Rice Husk Ash.

### 2.3 Silica extraction

Silica was extracted from Rice Husks Ash (RHA) after each burning at different temperature, by adapting the method of Kamath and Proctor [6], 250ml portions of 1 N NaOH were added to 50g of grounded RHA samples and boiled in a covered 500ml beaker for 1 hour with constant stirring using magnetic stirrer to dissolve the silica and produce a Sodium Silicate solution as in equation 1. The

solutions were filtered through Whatman No.41 ashless filter paper after the solution was allowed to cool to room temperature.

Deionized water was added to residue silicate solution to get the pH up to 11. Acidic solution of hydrochloric was prepared by adding 6M hydrochloric acid (HCl) to 100ml of deionized water until pH 1.5 was reached. The acidic solution was added with constant stirring to silicate solution of pH 11 until pH 4 was reached, see equation 2 for reaction and gel formation was promoted by incubating it at room temperature for overnight.



The silica gels produced were crushed inside the beakers, dispersed in deionized water of 100ml and the slurry was centrifuged at 5000rpm for 10min to remove soluble salt, the supernatant were discarded and the gels were subjected to washing and then dried at 80°C for 24 hours to obtain pure powder silica.

### 2.4 Moisture content of silica gels:

1 gram portion of gel produced after washing were heated in aluminium moisture pans at 130°C for 1 hour. The samples were cooled in a desiccators and weighed. The weight percent loss were recorded as the moisture content of samples.

### 2.5 Analyses/characterization:

#### 2.5.1 X-ray diffraction (XRD).

Patterns of ground silica powder samples were obtained by using a Bruker Advanced X-ray Solution D8 Advance at Life Sciences and Bioengineering Center of Worcester Polytechnic Institute (WPI) MA, USA. Using an acceleration voltage of 40KV and current of 40mA. 2-Theta was scanned from 5° to 55°, at a scanning speed of 2sec/step in the increment of 0.05.

#### 2.5.2 Energy Dispersive X-ray and Scanning Electron Microscopy.

FEI Quanta 200 FEG MKII scanning electron microscope with an Oxford –Link Inca 350 x-ray spectrometer with a 30 mm<sup>2</sup> window for light element detection and spectral imaging and phase analysis was used.

The powder samples of RHA were coated with carbon to ensure a conducting surface to obtained electron bombardment and characterization for elemental analysis and followed with scanning electron

microscope which was used to characterize the particle morphologies of the samples.

#### 4. Results and Discussions.

##### 4.1 Thermal decomposition.

Rice Husk Ashes in the furnace was allowed to cool down overnight. The ashes collected is gray to white in colour. After 7 hours of burning 1000g of rice husk each for sample A to F at various temperature the percentage loss in weight is summarized in table 2 showing that rice husk has 18 to 20 percent of ash.

Table 2: Different burning temperature of rice husk

RH sample	T(°C)	Ash weight(g)	% loss	Ash colour
A	650	192.6	80.74	White
B	600	180.3	81.97	White
C	550	181.7	81.83	White
D	500	184.0	81.60	White
E	450	181.9	81.81	gray
F	400	194.2	80.58	White
				gray

##### 4.2 Silica extraction and Moisture content.



Figure 2: Extracted silica in Al pan ready for drying.

Table 3. Percentage of compound in the RHA.

AT	AU	BT	BU	Formula
-	-	-	10.71	CO <sub>2</sub>
100	95.54	97.89	87.34	SiO <sub>2</sub>
-	1.35	-	1.08	P <sub>2</sub> O <sub>5</sub>
-	-	-	-	SO <sub>3</sub>
-	1.89	-	0.88	K <sub>2</sub> O
-	1.22	2.11	-	CaO

AT: sample A treated, AU: sample A untreated, BT: sample B treated and BU: sample B untreated.

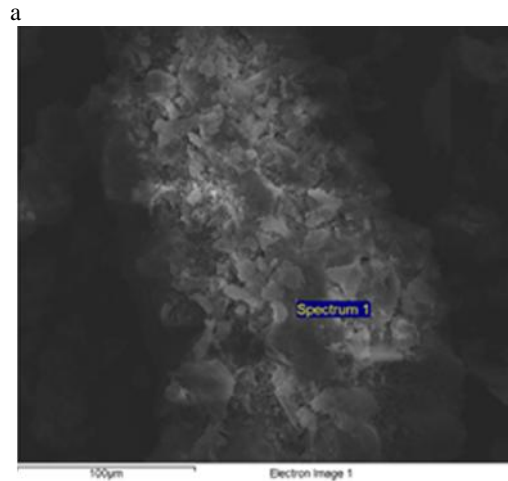
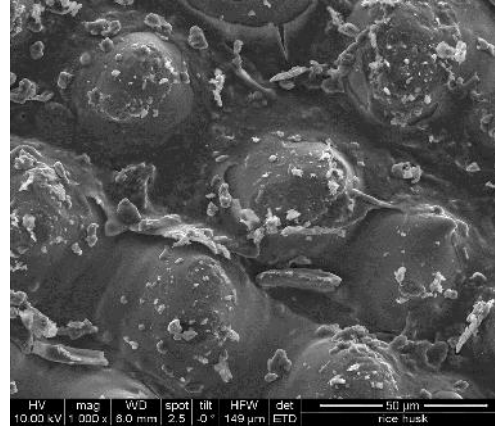
The figure 2 shows the extracted silica in aluminium pan ready for drying while table 3 and table 4 summarized the result of silica derived from rice husk ash and its moisture content respectively.

Table 4. Moisture content of RHA.

RHA sample	Weight after drying(g)
A	0.21
B	0.14
C	0.23
D	0.14
E	0.13
F	0.16

##### 4.3 Analyses

###### 4.3.1 Scanning Electron Microscopy.



b

Figure 3: SEM of (a) rice husk and (b) treated rice husk ash gotten at 650°C.

The untreated RH silica has the unique 3D porous structure that comes from the outer epidermis of natural rice husks. SEM image of RH in figure 3(a) reviews RH silica from outer surface of a rice husk at low magnification. The image confirms that the nanoporous structure is well organized. The morphological feature treated RHA at 650°C is shown in figure 3(b). From the figure 3(b) the RHA shows a porous and multifaceted particle shape and size. Knowing that the main components of rice husk includes silica, cellulose, hemi-cellulose, and lignin

[1]. The porous and honeycomb morphology seen in the figure 3(b) can be attributed to the burning out of the organic components in the rice husk during combustion. The solid hydrated silica subsequently polymerizes to form a skeletal silica network which may explain the flaky and honey comb-like structure in the SEM picture of figure 3(b).

#### 4.3.2 X-ray diffraction (XRD)

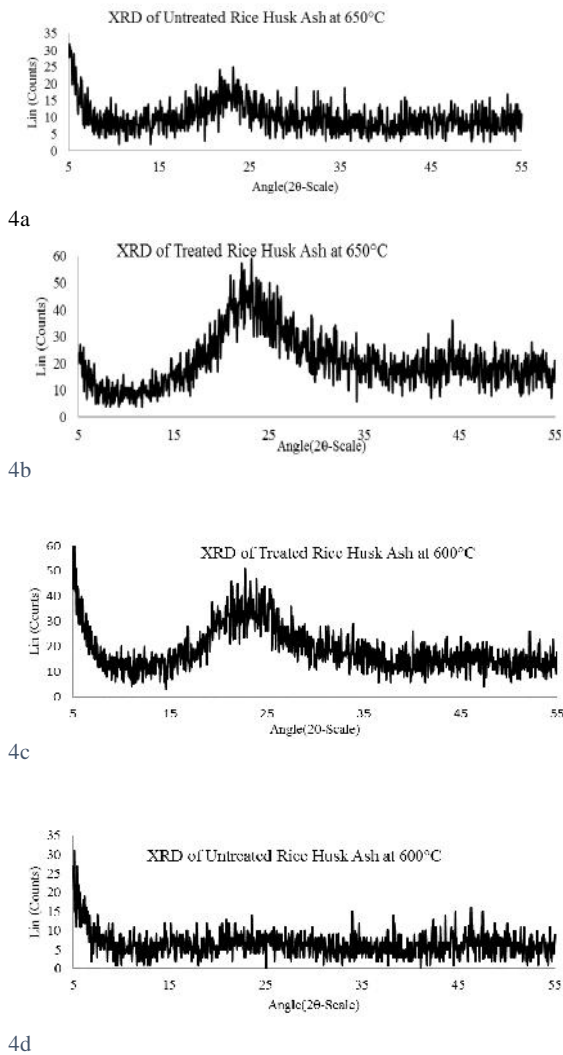


Figure 4: X-ray diffraction spectra of rice husk ash at 650°C to 600°C for the treated and untreated are shown.

The reactivity and health issue of silica is based on its crystal structure. Crystalline silica is less reactive to chemical treatment and may serve as carcinogenic while the amorphous silica is rather very reactive and with no harmful effect to human [15]. The comparison XRD spectra of the untreated and treated RHA at 650°C and 600°C are shown in figure 4a, 4b, 4c and 4d respectively. From the figure 4a, 4b, and 4c a broad peak spanning 2-theta angle range of 22.75 to 23.15

degree confirms the amorphous nature of silica from rice husk. RHA gotten at 650°C shows broad peak of 2-theta of 23.15 degree both on the untreated and treated with a line count difference of 29.

#### 4.3.3 Energy Dispersive X-ray

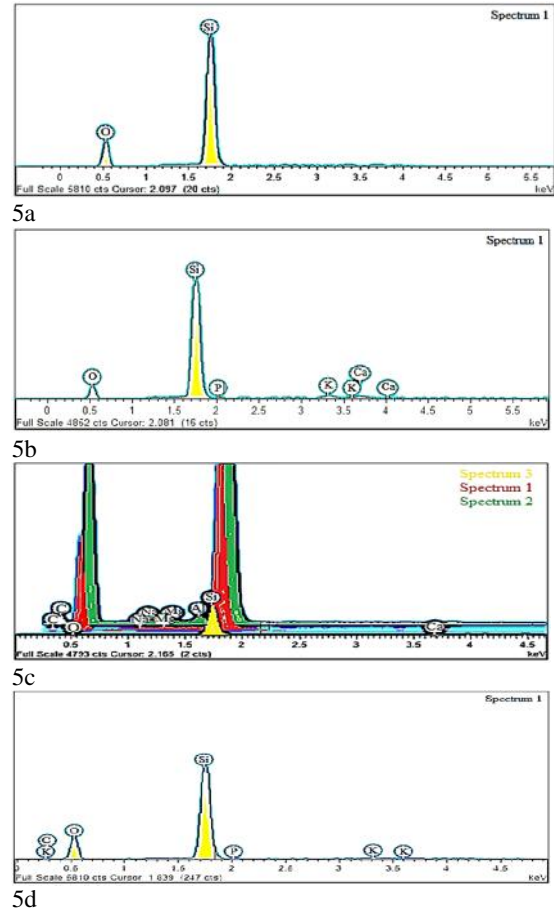


Figure 5: EDX of treated and untreated RHA at 650°C (5a and 5b) to 600°C (5c and 5d) respectively.

It is observed that the burning of RH to RHA at 650°C was more effective for elements (carbon, calcium, potassium, and phosphorus) removal than at 550°C and 600°C at table 2 and table 3 for ash colour change and compound percentage respectively. The EDX spectra of points identified are shown in figure 5d and 5c for RHA gotten at 600°C (untreated and treated) and in figure 5b and 5a for RHA at 650°C (untreated and treated). The analysis revealed a high silica rich solid with porous and sponger or honeycomb morphology. See table 3 for the percentages of silica extracted after burning followed by chemical treatment was much higher at 650°C. Before chemical treatment the ash gotten at 650°C has shown that you can have purity silica as observed in XRD and EDX and when treated with chemical you have a much more high-purity amorphous silica.

## 5. Conclusions

It was observed that after the thermal decomposition of RH at various temperature silica was extracted during the chemical treatment but a high purity amorphous silica was gotten at 650°C for sample A. And from analysis it agreed with literature that rice husks have lots of silica when burnt in the presence of air. Extensive work is still required in order to gain sufficient knowledge and understanding in silica extraction by varying the pH levels and silica reduction to silicon for solar cell production. Also, extensive work on burning RH at 650°C and varying the burning time should be done knowing fully well that it is more advantageous to work with amorphous silica than crystalline silica from quartz.

## Acknowledgments.

The authors would like to thank National Agency for Science and Engineering Infrastructure (NASENI)-WORLD BANK STEP B program and the Africa University of Science and Technology (AUST) Abuja Nigeria for their financial support. The efforts of technical staff of Civil and Environmental Engineering, Worcester Polytechnic Institute MA, USA is also acknowledged.

## References.

1. Biyi Daramola (2005) Government Policies and Competitiveness of Nigerian Rice Economy. Workshop on Rice Policy & Food Security in Sub-Saharan Africa' organized by WARDA, Cotonou, Republic of Benin.
2. A. Muthadhi, "Studies on Production of Reactive Rice Husk Ash and Performance of Rha-Concrete" (Ph.D. thesis, Pondicherry University, 2010), 7.
3. S. J. Dae, H. R. Myung, J. S. Yong, B. P. Seung and W. C. Jang, "Recycling rice husks for high-capacity lithium battery anodes", [www.pnas.org/cgi/doi/10.1073/pnas.1305025110](http://www.pnas.org/cgi/doi/10.1073/pnas.1305025110).
4. Nian Liu, Kaifu Huo, Matthew T. McDowell, Jie Zhao & Yi Cui (2013) Rice husks as a sustainable source of nanostructured silicon for high performance Li-ion battery anodes, *Scientific reports*
5. E. A. Okoronkwo, P. E. Imoisili, S. O. O. Olusunle (2013) Extraction and characterization of Amorphous Silica from Corn Cob Ash by Sol-Gel Method. [www.iiste.org](http://www.iiste.org)
6. U. Kalapathy, A. Proctor, J. Shultz (2002). An improved method for production of silica from rice hull ash. 2002 Elsevier Science Ltd.
7. Prasad, C. S., Maiti K. N., and Venugopal, R., (2000), "Effect of RHA in white ware composition", *Ceramics International*, Vol.27, pp. 629-635.
8. Bouzoubaa, N., and Fournier, B., (2001), "Concrete incorporating rice husk ash: Compressive strength and chloride ion penetrability", *Materials Technology laboratory, CANMET, Department of Natural resources, Canada*, pp. 1-16.
9. Alexis T. Belonio, *Rice Husk Gas Stove Handbook* (Central Phillippine University, Iloilo City, Phillippines 2005), 15-17.
10. Stroeven, P., Bui, D. D., and Sabuni, E., (1999), "Ash of vegetable waste used for economic production of low to high strength hydraulic binders", *Fuel*, Vol. 78, pp. 153-159.
11. Hwang, C. L., and Chandra, S., (1997), "Waste materials used in concrete manufacturing", *William Andrew. inc*, pp. 184-234.
12. Asavapisit, S., and Ruengrit, N., (2005), "The role of RHA blended cement in stabilizing metal containing wastes", *Cement and Concrete Composites*, Vol.3, pp.782- 787.
13. Basha, E. A., Hashim, R., Mahmud, H. B., and Muntohar, A. S., (2005), "Stabilization of residual soil with RHA & cement", *Construction and Building Materials*, Vol.19, pp. 448-453.
14. Shomglin, K., Monteiro, P., and Harvey, J., "Accelerated laboratory testing for high early strength concrete for alkali aggregate reaction", (M.Eng. thesis, *Department of Transportation, California*, 2001).
15. K. K. Larbi, "Synthesis of High Purity Silicon from Rice Husks" (M.Eng. thesis, *University of Toronto*, 2010), 50-65.

# Acoustic Study of Insulators Manufactured from Textile waste : The case of the Tablecloth Structure

A.Haddad, F. Fayala, S. BenLtoufa and A. Jemni  
Laboratory Studies of Thermal and Energy Systems (LESTE), National School of  
Engineering of Monastir (ENIM), Monastir University  
Avenue Ibn Eljazzar Monastir 5019 TUNISIA

## Abstract:

This work presents a pursuit of thermal and acoustic insulation study of a manufactured material made of textile waste shredded in two structures: tablecloth and linters, which can provide thermal and sound insulation of buildings. In this section, we measure the sound settings precisely its sound absorption coefficient  $\alpha$ , its coefficient acoustic reflection  $R$ , its impedance  $Z$  and the parameters in conjunction: air permeability,  $\sigma$ , and density  $\rho$ . A comparative study with other civil building materials was thus carried out.

Keywords: Textile waste, acoustic insulation, sound absorption coefficient, coefficient acoustic reflection, building materials, acoustic impedance.



Figure 1: Presentation of the material to be examined

- a Sample Textile Waste: linters structure
- b Sample textile waste: tablecloth structure
- c Sample textile waste: enlarged image

## I. Introduction

Textiles are one of the fastest growing waste product (In Europe and America, it is estimated that 10 million tonnes of textiles are discarded every year<sup>1</sup>. In China the total annual production of pre and post-consumer

textile waste is estimated to be over 20 million tonnes<sup>2</sup>) and the wastes cause both health and environmental problems, so that, this has forced governments to search solutions and develop laws for recycling. The first approach to our waste challenge is to cut the creation of waste in the first place, it's the **Reduction**; the second approach is the **Reuse** and the third approach is the **Recycling**.

In the other hand, the noise pollution is a problem that becomes more pronounced with time. Likewise, the accumulation of generated waste and the need of waste management becoming increasingly important. In this study, we describe a new material made from textile waste. In fact, textile waste, traverse the shredding process, transforms itself into linters then in tablecloth of desired thickness. These two structures can be applied in thermal and acoustic insulation of buildings. This part presents a study of the acoustic insulation of tablecloth textile waste and of some associated parameters: density and air permeability, [2], [3], [4].

Porous absorbent materials include hard and soft materials and all have one important thing in common-their network of interlocking fibers and pores. Materials with closed cells such as the foamed plastics are usually far less effective as sound absorbers[6].

## II. Material and Methods

### I.1. Materials

Textile waste are combined, without selection, comminuted, then scour the process of setting tablecloth, thereby obtaining a volume of selected variable thickness structure formed by fibers and sometimes small pieces of fabric and knit which will curl on an output roller. Fig.1 (b) presents a sample of the material tablecloth in question; an enlarged image is showed in 1 (c).

### I.2. Methods

before each test, the samples have to be conditioned in a climate chamber for a long time, exceeding 24 hours. Temperature and humidity are adjustable and their values are selected according to the measurement standards.

#### I.2.1. Acoustic parameters

##### I.2.1.1. Device

To determine the acoustic parameters, was used a Kundt tube with one microphone. A sound wave is emitted from the tube extremity, where is positioned the acoustic source, the specimen is paced at the other tube extremity. A reflected wave then propagates in reverse. The two waves together form antinodes and troughs that will be detected using a micro movable along the OX axis connected to an amplifier and an oscilloscope to. For each frequency,  $f$ , we measure the maximum and minimum amplitudes and the wavelength,  $\lambda$ , through the antinodes and troughs waves encountered during displacement of the microphone. The device is as the following,

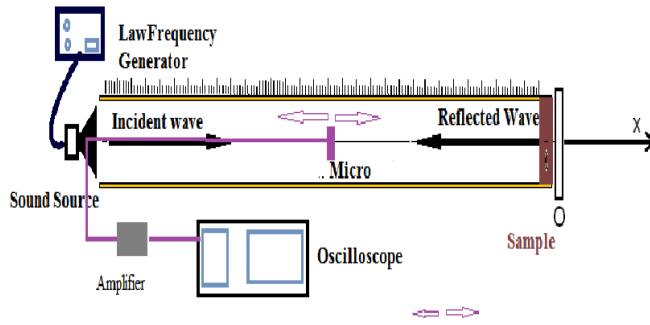


Figure 2: The kundt Tube

There is a graduated glass tube from 34 cm of diameter and 1 m of length. the sample is placed in a tube extremity; while the source is placed at the other extremity. Law Frequency Generator, LFG, generates a sound wave frequency with adjustable value that can varied from 10 to 10.000 Hz. The microphone, sound sensor, moves slowly along the axis OX and detects the antinodes and troughs sound. it sends thereafter, the signal to the amplifier which transmits it to the oscilloscope.

### I.2.1.2. Theoretical analysis

Sound waves are longitudinal elastic vibrations. When a sound wave passes through tube filled with a homogeneous fluid, its passage causes a local change in pressure, and induces displacement of the particles of fluid about their equilibrium positions. It is shown that the displacement fluid molecules; the pressure variation; and the fluid velocity of the molecules are not independent and obey the same propagation equation. if we know the wave speed  $v$ , the pressure wave  $p$  is determined by the relationship  $p = \rho cv$ . For the case of a Kundt tube (closed tube), the incident wave  $W_i$ , emitted by a source placed at the end of the tube interferes with the reflected wave  $W_r$  by the specimen, placed at the other extremity, at any point M located at a distance  $x$  of O, Figure 2, we can write: [1], [5], [7]

$$V_i^*(x, t) = Ae^{-j\omega(t-\frac{x}{c})} \quad \text{eq.1}$$

$$V_r^*(x, t) = R^* Ae^{-j\omega(t-\frac{2L-x}{c})} \quad \text{eq.2}$$

$$V(x, t) = V_i^*(x, t) + V_r^*(x, t) = Ae^{j\omega(t-\frac{x}{c})} [1 + R^* e^{-2j\omega(\frac{L-x}{c})}] \quad \text{eq.3}$$

In this expression, we deduce that the pressure

$$P^*(x, t) = \rho C Ae^{j\omega(t-\frac{x}{c})} [1 - R^* e^{-2j\omega(\frac{L-x}{c})}] \quad \text{eq.4}$$

At the end of the tube,  $y = 0$  at the distance  $y = L - x$  of the terminating of the pipe, the expression of  $p$  becomes:

$$P^*(x, t) = \rho C Ae^{-j\omega(t-\frac{x}{c})} [1 - |R| e^{j(\theta-4\pi\frac{y}{\lambda})}] \quad \text{eq.5}$$

This wave therefore, presents minimum amplitude  $|P_{min}| = A(1-R)$  for the following values of  $x$  that verify :

$$\frac{2\pi}{\lambda}x = n\pi, \quad \text{thus } x = n\frac{\lambda}{2}; n = 1, 2, 3, \dots \quad \text{q.6}$$

And maximum amplitude  $|P_{max}| = A(1+R)$  for the following values of  $x$  then

$$\frac{2\pi}{\lambda}x = (2n+1)\frac{\pi}{2}, \quad \text{thus } x = (2n+1)\frac{\lambda}{4}; n = 1, 2, 3, \dots \quad \text{eq.7}$$

It may be noted that the distance between two consecutive maxima (called also "antinodes pressure") or two consecutive minima ("pressure nodes") is equal to  $\lambda/2$ . The reflection coefficient  $R$  is given by the expression  $R = (P_{max}-P_{min}) / (P_{max} + P_{min})$  eq.8

The sound absorption coefficient,  $\alpha$  is given by:

$$\alpha = 1-R^2 \quad \text{eq.9}$$

The impedance is a sinusoidal function, and we can calculate the reduced impedance  $Z$

$$Z = \rho c \frac{P_{max}}{P_{min}} \quad \text{eq.10}$$

$\rho c$  is the acoustic impedance air, this is equal to 415.3. The frequency must be limited by a minimum frequency and maximum frequency:

- The length of wave,  $\lambda$ , should not exceed th length of the tube  $L$ ,  $L < \lambda$ , with  $\lambda = \frac{c}{f}$

which implies that

$$f < \frac{c}{L}$$

$C$  is the speed of the wave in air, is 343 m / s, the length  $L$  of the tube is equal to 1 m So  $f < 342$  Hz.

- On the other hand, the internal acoustic field can be considered unidirectional for frequencies lower than the cutoff Frequency  $f_c$

$$f_c < 1.84 \frac{c}{2\pi r}$$

Which,  $f_c$ , in our case is about 5894Hz;  $r$  is the tube radius.

### I.2.3. Air permeability

The sample is placed between a moveable jaw and a cylinder of diameter equal to 20 cm connected to the air compressor, as shown in Figure 4. The jaw is tightened securely to prevent loss of air flow through the sample. Sensors measure the pressure drop across the sample; the value of the air permeability,  $\sigma$ , is thereby displayed directly. This device is based on the standard G07-111-ASTM D 737, BS 5'636

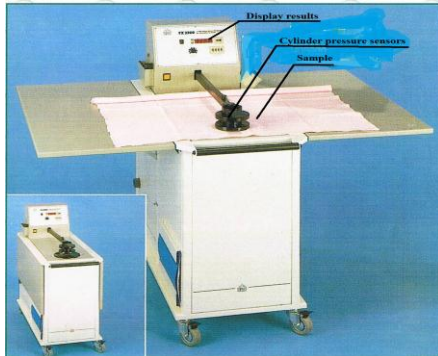


Figure 3: Air permeability tester

### I.2.4. Density

The density of the sample is determined in laboratory by the weighed method. The used volume is  $2916 \cdot 10^{-6} \text{ m}^3$ , the conditioned mass of the specimen is 155.476 g, which gives a density of  $53.31 \text{ kg/m}^3$ .

## III. Results and discussions,

The associated parameters are summarized in Table 1 below

Table 1 parameters influencing the sound absorption	
Density $\rho$ ( $\text{kg} / \text{m}^3$ )	53.31
Air permeability $\sigma$ ( $\text{l/m}^2/\text{s}$ )	381.33

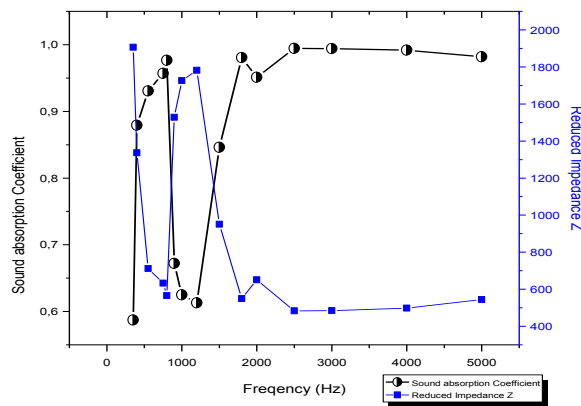


Figure 4: curve of sound absorption coefficient,  $\alpha$ , and Reduced Impedance  $Z$ .

The sound absorption coefficient,  $\alpha$ , is always greater than 0.5. it exceeds 0.9 for frequencies above 1800 Hz. Sound absorption curve shows peaks and variable amplitude frequency position; a first peak reaching its remarkable minimum for a frequency 1200 Hz, and is set to 0.6; a low second peak for the frequency 1200 Hz has been detected, for which  $\alpha$  is equal to 0.95.

For a frequency between 350 Hz and 800 Hz, the sound absorption increases with frequency up to reach 0.97. it undergoes a major peak in the frequency band between 800 and 1800, a low peak between 1800 and 2500 and then stabilizes in the vicinity of 0.99 for the rest of the frequencies range studied.

The existence of noise peak can be explained by two reasons:

- the first is a diffraction phenomenon that occurs if the wavelength is the same order as the size of pores on the surface. In our case, for the frequency 1200  $\lambda$  is 0.28 m and for the frequency 2000,  $\lambda$  is equal to 0.16m, so incomparable with the pore size that does not exceed a few millimeters.

- The second reason is due to the fact that if the material has a single characteristic pore size, it says single porosity. Fluid flow can be characterized by the equation of Navier stocks and we can calculate at any point of the network fluid pressure. So the sound absorption coefficient,  $\alpha$ , increases in a regular manner with the frequency. However, the existence of two sizes of pores characteristic changes the global acoustic behavior of the material. We distinguish the macro pores and micropores. Or the pressure in the two types of pores are different. Diffusion phenomena between the two networks overlap with wave propagation phenomena so, we can observe absorption peaks.

In the other hand, during the sollicitation of fluid inside the pores, the air undergoes cycles of compression / relaxation, its temperature therefore varies unlike solid which retains its temperature constant. It appears a layer, which characterizes the thickness of the fluid from the walled on which the temperature distribution is disturbed. if  $b$  designe the thickness of this layer then its value varies with frequency according to the following relationship:

$b = D / w$ ;  $D$ : thermal diffusivity,  $w$ : pulsation.

- For  $b \ll r$ , high frequencies,  $r$  is the radius of the tube, so the stress cycle is fast enough that the transformation is considered adiabatic and the insulation is maximized.

- If  $b \gg r$ , where low frequencies, the cycle is slow enough that the transformation is isothermal. This thermal effect also explains why the absorption is starting with a low value and then increases until stable for a wide range of frequencies.

This impedance has a significant peak for the frequency of 1200, it is 1782. Another peak is observed for  $f = 2000$ , the corresponding impedance is 650 reynolds.

These peaks are due to the non-uniform porosity of the structure.

The impedance characterizes the sound resistance absorption of material and with respect to these measures, our material is a good acoustic insulator. It have an impedance comprised between 500 and 2000 Reynolds.

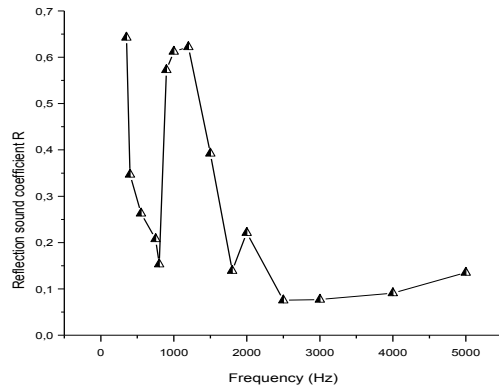


Figure 5: curve of reflection sound coefficient R

The sound absorption coefficient indicates that the reflection of the sound pressure is around 70% at the beginning, it decreases with frequency until reaching about 15% for frequencies, superior to 2500 Hz. This curve has, also, two peaks at the same frequencies. This behavior can be explained by the same reasons.

#### IV. Comparison

The thick glass wool TGW was studied [7], we note that for TGW The sound absorption coefficient started with 0.2 and keep low values for frequencies up to 700 Hz.  $\alpha$  in our case is always greater than 0.5. The impedance range for TGW is similar to that of the studied material, they both have similar curves and they have a low resistance to sound absorption

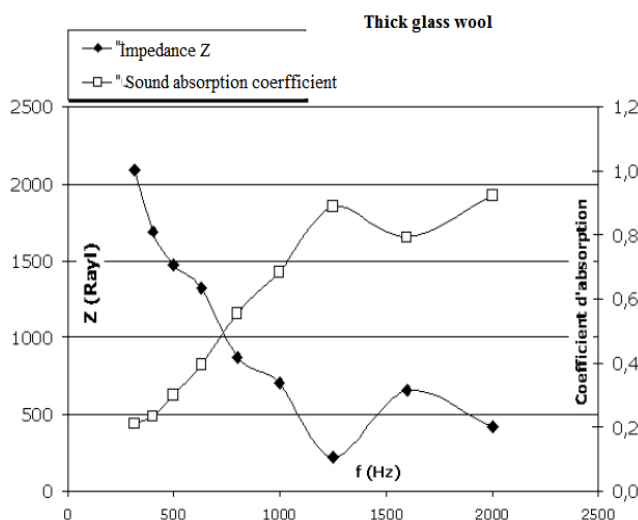


Figure 6: Reduced Impedance and sound absorption coefficient curve [7].

#### V. Conclusion

The tablecloth material of textile waste was studied. And compared with TGW. It has reduced impedance between 544 and 1900 Raylds. It has a low resistance to the sound absorption. Its resistance is approaching that of TGW

Its sound absorption coefficient,  $\alpha$ , is always superior to 0.5, it have a value exceeding 0.95 over the entire frequency range beyond 1800 Hz. So is better than TGW.

The reflection sound coefficient is in the order of 0.1 to 0.2 over the majority of the frequencies (high frequencies, from 1800 onwards Hz)

Structural criteria of the material affect the sound parameters and we can conclude that the material haven't a uniform porosity.

There is a range of frequency for which the acoustic absorption is great. High frequencies promotes sound absorption.

The tablecloth material of textile waste can be a competitive acoustic insulator compared to TGW and other materials.

This work can be completed by the study of the relation between the acoustic parameters,  $\sigma$ ,  $\rho$ ,  $\Phi$ , T, E and the acoustic absorption.

#### VI. Abreviations

Aabbreviations	
$\alpha$	Sound absorption coefficient
$z$	Impedance (rayld)
$\sigma$	Air permeability ( $l/m^2/s$ )
$v$	Wave speed (m/s)
$p$	Sound pressure (Pa)
$\rho$	Air density at 25 °C, is equal to $1.21 \text{ kg/m}^3$
$C$	Celerity of sound wave in air it's 343 m/s
$A$	constant
*	complex form
$R$	Coefficient acoustic reflection
$w$	pulse of the sound wave (rad/s)
$t$	time(s)
$x$	distance beteenw the origin and the position of micro, M.(m)
$L$	Tube length(m)
$\Theta$	phase shift between the wave emitted and Reflected(rad)
$\lambda$	wavelength(m)
$\Pi$	constant = 3.14
$n$	integer
$   $	absolute value
$R$	Tube radius(m)
$f_c$	Cuoff frequency (Hz)
$D$	Thermal diffisivity
$\Phi$	Porosity
$T$	Tortuosity
$E$	Emissivity
TGW	The Thick Glass Wool

#### VII. References

[1] Jiri Z., Azra K., Vit P., Jitka H. and Thomas B. (2012) Performance evaluation and research of alterna-

tive thermal insulations based on sheep wool, *Int. J. Energy and building*, 49,246-253

[2 ] El Hajja N., Mboumba-Mamboundoua B., Dheilily R., Abourab Z., Benzeggagh M., Queneudeca M., (2011)Development of thermal insulating and sound absorbing agro-sourced materials from auto linked flax-tows *Int. J. Industrial Crops and Products*, 34,921-928

[3 ] Jimenez-Espadafor F.J., Villanueva J.A.B., Torres García M., Carvajal Trujillo E., Muñoz Blanco A, (2011) Optimal design of acoustic material from tire fluff, *Int. J. Materials and Design*, 32,3608-3616

[4 ] Fouladi M.H, Jailani Mohd Nor M., Ayub M, Ali Leman Z., (2010) Utilization of coir fiber in multilayer acoustic absorption panel , *Int. J. Applied Acoustics*, 71, 241-249

[5 ] Binici H., Aksogan O., Bakbak D., Kaplan H., Isik B., (2009) Sound insulation of fibre reinforced mud brick walls, *Int. J. Construction and Building Materials*, 23, 1035-1041

[6 ] Atalla N., Amédin C.K., Atalla Y., Panneton R., Sgard F., (2004) Development of new absorbent materials with high acoustic performance to reduce noise at low frequencies, studies and research of Research Institute Robert-Sauvé Occupational Health and Safety (IRSST) of Montréal (Québec)

[7] Marchesse Y., (2010-2011) Introduction a l'acoustique. Mechanics and Energetics departement, Unit Teaching S8UP1 , Catholic school of arts and crafts of Lyon, France

# Effects of collector slope on solar chimney power plant performances

H. Atia,<sup>1</sup> A. Ilinca,<sup>2</sup> A. Snoussi,<sup>1</sup> R. Boukchina,<sup>3</sup> A. Benbrahim,<sup>1</sup>

<sup>1</sup>University of Gabes, National Engineering School of Gabes, Applied Thermodynamic Research Unit(UR11SE80), Tunisia

<sup>2</sup>Wind Energy Research Laboratory, Université du Québec à Rimouski, Rimouski, Canada

<sup>3</sup>Arid Regions Institute (IRA), Gabes, Tunisia

## Abstract

A CFD analysis using ANSYS Fluent software was conducted to study the effects of collector slope on solar chimney's performances. Three solar chimney configurations, named A, B and C, which correspond to a slope of 0°, 2.5° and 5°, respectively, were studied. Both collector Radius and chimney height were fixed to 495m for the three configurations. For the three studied configurations, the pressure ratio was fixed to 0.9 and the solar radiation was varied from 200 W/m<sup>2</sup> to 1100 W/m<sup>2</sup>.

The results show that the thermodynamic performances of the solar chimney were enhanced by increasing the inclination angle of the collector roof. For instance, the work extracted from configuration A, B and C were, respectively, 2.33, 8.46 and 10.11 MW for a solar radiation of 1100 W/m<sup>2</sup>. The thermal efficiency increases from 0.3% to 1.25%, while, the exergetic efficiency vary from 0.69% to 1.82% when the inclination angle is varied from 0 to 5°.

Keywords: solar chimney, collector roof slope, therm efficiency, exergetic efficiency, work extracted.

## 1. Introduction

Solar chimney is a promising process for renewable electricity production due to its simplicity and easiness of maintenance. It consists of three components, namely, a solar collector, a chimney and a turbine generator.

Many research works were conducted to find the best combination of the geometrical parameters leading to power maximisation in the solar chimney (Li, Guo et al. 2012, Koonsrisuk 2013, Koonsrisuk and Chitsomboon 2013, Dehghani and Mohammadi 2014, Lebbi, Chergui et al. 2014, Patel, Prasad et al. 2014).

In this work, we focused on studying the effects of collector slope on solar chimney performances.

## 2. Computational work

In this work, three solar chimney configurations, where the design parameters are detailed in table.1, were studied.

Table 1. Design parameters for the studied configurations

configuration	Inclination (°)	Collector radius(m)	Chimney height(m)
A	0	495	495
B	2.5	495	495
C	5	495	495

The simulations were conducted for steady flow using the commercially available CFD package (ANSYS Fluent). The problem is considered axisymmetric. The SIMPLEC algorithm was used to resolve the fluid and the heat transfer equations. The standard k-ε model is used in all simulations. The green house effect in the collector is modeled using the discret ordinate model.

The power extracted from the turbine is calculated using equation 1 (Fasel, Meng et al. 2013)

$$\dot{W}_{ext} = \frac{\dot{m}}{\rho_{avr}} \Delta P_{turb}$$

The overall efficiency and the exergetic efficiency were calculated using equations (2-4).

$$\eta_{overall} = \frac{\dot{W}_{ext}}{IA_c}$$

$$\eta_{ex} = \frac{\dot{W}_{ext}}{\dot{W}_{rev}}$$

Where:

$$\dot{W}_{rev} = \dot{m} \left( (H_1 - H_4) + T_1(S_4 - S_1) + \frac{1}{2} (V_1^2 - V_4^2) - g(h_{ch} + h_{cool}) \right) + \left( 1 - \frac{T_1}{T_{avr,c}} \right) IA_c$$

## 3. Results and discussion

The inclination angle of 2.5° and 5° lead to an increase of the collector area of 0.024% and

0.095 % respectively. In addition, it leads to an increase of the collector outlet section, thereby, a demunition of the turbulence in this region.

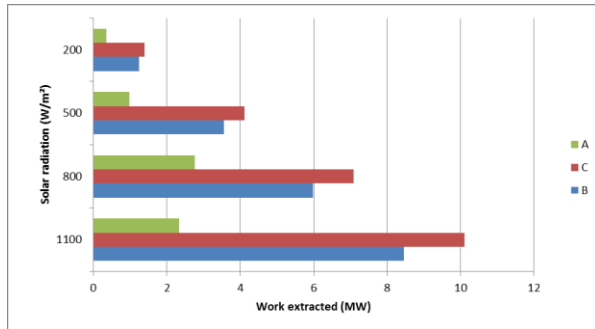


Fig1. Comparison of the work extracted from the three studied configurations A, B and C at various solar radiation values.

Fig.1 shows that the work extracted increases by increasing the collector slope and the solar radiation. For instance, the work extracted from configuration A, B and C were, respectively, 2.33, 8.46 and 10.11 MW for a solar radiation of 1100 W/m². While, it varies from 1.39 to 10.11 when the solar radiation moves from 200 W/m² to 1100 W/m² for configuration C.

Fig.2 shows the overall efficiencies of various configurations at various solar radiations. The efficiencies of the solar chimney power plant are very low, however, the solar energy is free. It can be noted that the overall process efficiency increase with increasing solar radiation and inclination angle. For configuration A, the overall efficiency achieves a maximum at a solar radiation of 800 W/m². This could be explained by the increase of turbulence in the collector outlet section.

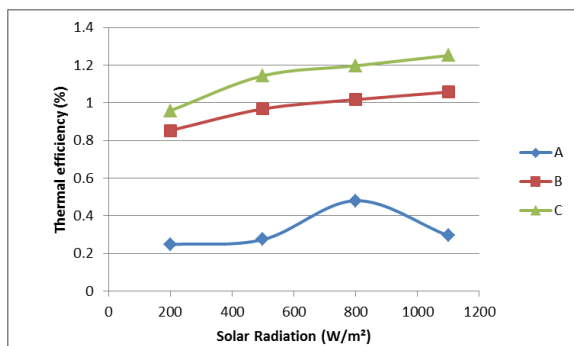


Fig 2. Comparison of the thermal efficiencies of the three studied configurations A, B and C at various solar radiation values.

The exergetic efficiency, represented in fig.3 is directly influenced by the solar radiation value which confirms the previous results that shows that the sloped solar chimney has better performances than the conventional one.

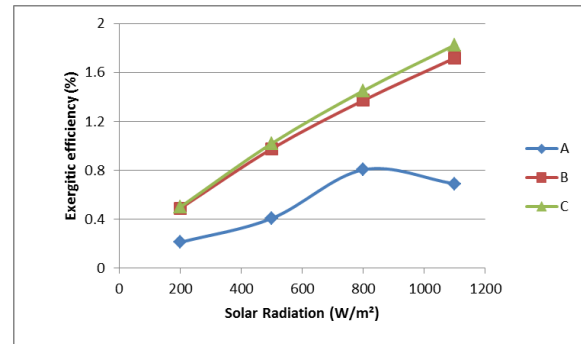


Fig3. Comparison of the exergetic efficiencies of the three studied configurations A, B and C at various solar radiation values.

#### 4. Conclusion

According to this study, it is shown that the increase of the collector slope enhances dramatically the solar chimney performances. Thus, the power extracted is strongly increased. And the collector area is increased without increasing the occupied land.

As a perspective other geometrical and radiative parameters should be considered for SSPP evaluation

#### Acknowledgements

this project is in the framework of a PhD thesis MOBIDOC of PASRI program funded by the European Union and administered by the ANPR.

#### References

- Dehghani, S. and A. H. Mohammadi (2014). "Optimum dimension of geometric parameters of solar chimney power plants – A multi-objective optimization approach." *Solar Energy* **105**(0): 603-612.
- Fasel, H. F., F. Meng, E. Shams and A. Gross (2013). "CFD analysis for solar chimney power plants." *Solar Energy* **98, Part A**(0): 12-22.
- Koonsrisuk, A. (2013). "Comparison of conventional solar chimney power plants and sloped solar chimney power plants using second law analysis." *Solar Energy* **98, Part A**(0): 78-84.
- Koonsrisuk, A. and T. Chitsomboon (2013). "Effects of flow area changes on the potential of solar chimney power plants." *Energy* **51**(0): 400-406.
- Lebbi, M., T. Chergui, H. Boualit and I. Boutina (2014). "Influence of geometric parameters on the hydrodynamics

control of solar chimney." International Journal of Hydrogen Energy **39**(27): 15246-15255.

Li, J.-y., P.-h. Guo and Y. Wang (2012). "Effects of collector radius and chimney height on power output of a solar chimney power plant with turbines." Renewable Energy **47**(0): 21-28.

Patel, S. K., D. Prasad and M. R. Ahmed (2014). "Computational studies on the effect of geometric parameters on the performance of a solar chimney power plant." Energy Conversion and Management **77**(0): 424-431.

# Fuzzy Controller in Energy Storage for Improvement of Power Quality Issues with Renewable Energy and Electric Car

Khim Yan Lim,<sup>1</sup> Yun Seng Lim,<sup>1</sup> Jianhui Wong,<sup>1</sup> Kein Huat Chua,<sup>1</sup>

<sup>1</sup>Faculty of Engineering and Science, University Tunku Abdul Rahman, Jalan Genting Kelang, 53300 Kuala Lumpur, Malaysia.

**Abstract:** The integration of renewable energy sources (RE) into the low voltage (LV) networks can create a number of power quality issues. RE can cause voltage unbalance and low power factor when it injects real power into the network. Energy storage system can be connected to the network to accommodate the excess energy from RE with the supply of reactive power as a complementary support, hence correcting the voltage unbalance and power factor effectively without wasting any generated energy. To be able to correct the voltage unbalance and power factor effectively under the intermittent power of RE, a novel fuzzy controller is developed and implemented in the energy storage to manipulate the flow of real and reactive power between the energy storage and the network based on the network conditions. The fuzzy controller is able to reduce any voltage excursions with the use of real and reactive power from the energy storage, hence reducing the voltage unbalance and improving the power factor. Numerous experiments have been carried out to verify the effectiveness of the fuzzy controller. The experimental results show that the voltage unbalance and power factors are constantly maintained below the thresholds under the high intermittent power output of the photovoltaic systems.

**Keywords:** Renewable energy, Energy storage, Voltage Unbalance, Power factor, Fuzzy Controller, Electric Vehicle.

## Introduction:

Photovoltaic (PV) system is one of the potential renewable energy resources in Malaysia due to its abundant solar irradiance. The installation of single-phase PV systems are usually unplanned and customer driven. Malaysia is one of countries with the cloudiest skies. The solar irradiance under cloudy sky conditions is highly scattered, causing the PV power outputs to fluctuate substantially. The intermittent power outputs and the growth of PV systems on the LV network tends to raise several technical issues including voltage rise, voltage unbalance, voltage sag and voltage swell (Prakash K. Ray, 2013). Electric cars are a step closer to make the world a greener place. At present, electric cars are getting popular

among the country and the number is expected to grow in near future. There are 19 charging stations at present and another 300 charging stations will be installed by year 2015. Hence, power consumption will be increased tremendously and burden the network. There is a blackout happened in the United States and Canada in August 2003 due to insufficient of reactive power. This incident indicates that reactive power is important in maintaining the functionality of the transmission lines and distribution lines (Canada, 2004). Most generators have automatic voltage regulators that control the flow of reactive power to maintain voltages within required levels. Low voltage can cause electric system instability or collapse and, at distribution voltages, can damage motors and the disoperation of electronic equipment (Canada, 2004). In the public network, inductive loads such as induction motors, and generators consume reactive power causing low power factor and hence creating network power loss and reduce network efficiency. There are existing methods to overcome such issues by using static VAR compensator (SVC), static synchronous compensator (STATCOM), application of passive and active filters, and converters.

Therefore, reactive power compensation and problem solver for poor power factor is highly emphasized in these modern power distribution system. Controlling of reactive power also implies regulating the voltage, which is important for proper operation of an electric system (A. Jan von Appen, 2011). To solve these problems, energy storage system is integrated to the network to accommodate the excess energy from the renewable energy and it is effective to improve the power quality without wasting any renewable energy (Wong, Lim, & Morris, 2014).

In this paper, a novel fuzzy control algorithm is proposed not only to mitigate the voltage rise, and voltage unbalance, but also to supply reactive power as a complementary support for power factor correction.

## Experimental LV Distribution Network:

An experimental LV distribution network is developed to investigate the effectiveness of the fuzzy controller as shown in Figure 1. It consists of a network emulator, 3.6 kW<sub>p</sub> PV systems, a 9 kW three-phase load emulator and the fuzzy controlled energy storage system.

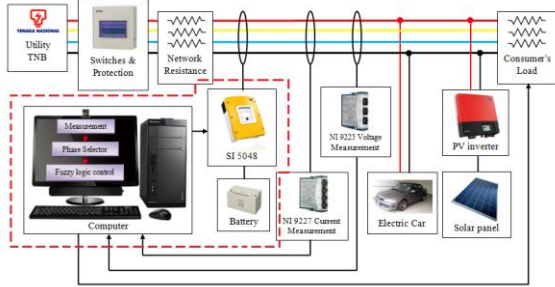


Figure 1: Experimental network diagram.

## Control Strategy of the Fuzzy Controlled Energy Storage System

The proposed energy storage system consists of three bi-directional inverters, namely Sunny Island 5048 (SI5048). Each SI5048 is integrated with four battery banks, while each bank consists of four valve-regulated lead acid (VRLA) batteries rated at 48 V, 115 Ah. Four banks are connected in parallel in order to increase the capacity to 460 Ah. A fuzzy control algorithm is developed in a supervisory computer to manipulate the real and reactive power flow of the energy storage system, so to mitigate voltage rise, voltage unbalance, and power factor. A monitoring system consists of voltage, current, and power measurements is developed. Several 40/5 A current transformers are used to measure current, whereas National Instrument, NI 9225 3-Channels Voltage Measurement Card is used for voltage measurement. Elcontrol STAR 3 power meters are used to display the parameters.

The fuzzy control algorithm is developed by using LabVIEW™ to manipulate the real and reactive power flow of the energy storage system. The fuzzy control method is mainly used to handle the fluctuating voltage rises and voltage unbalances that happen predominantly in Southeast Asia or other regions with cloudy sky. The proposed energy storage system is also capable to supply reactive power to correct low power factor on the distribution networks. Figure 2 shows the flow chart of the control algorithm.

The energy storage system manage to regulate the real power supplied or absorbed by using the proposed fuzzy logic control method effectively based on the varying voltage magnitude. This is proven experimentally where voltage magnitude is well controlled within a tolerated range, 238 V to 243 V, un-

der the high occasionally photovoltaic output power. In advanced, power factor dropped due to the inductive load can be improved by using this fuzzy logic control method to manipulate the amount of reactive power supplied based on the instantaneous power factor.

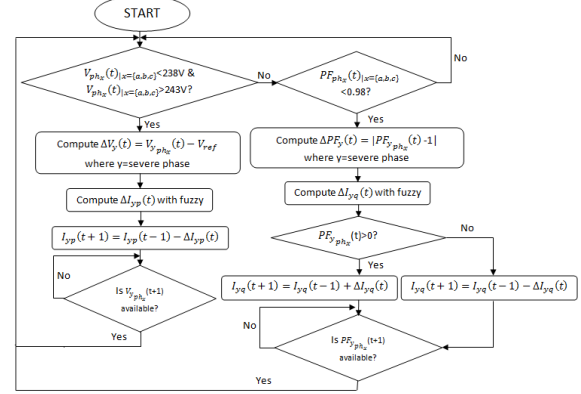


Figure 2: Flowchart of control algorithm.

The fuzzy control algorithm receives the measured voltage ( $V_{phx}$ ) and power factor ( $PF_{phx}$ ) in real time.  $V_{phx}$  is the measured voltage at the point of common coupling (PCC). Park's transformation is used to determine the voltage deviated severe phase. The system begins with the initial verification of the voltage by checking whether the three-phase voltages are well within the acceptable tolerance between 238 V and 243 V. Should the voltage is out of the range, the energy storage system will be activated to carry out the proactive action before voltage rise or voltage unbalance becomes severe. Voltage deviation,  $\Delta V_y$  is computed by using  $V_{yphx} - V_{ref}$ , where  $V_{yphx}$  is the measured voltage of the severe phase at the PCC and  $V_{ref}$  is the nominal voltage rated at 240 V. The fuzzy control uses  $\Delta V_y$  as one of the linguistic variables to create seven linguistic terms through fuzzification in order to generate one output ( $\Delta I_p$ ) as the instruction to the bi-directional inverter through defuzzification. The bi-directional inverter will adjust its real power output accordingly. This process will continue until the voltage magnitude is within the statutory limit. Once the voltage magnitude is restored, the voltage unbalance factor will also reduced.

Similarly, should the power factor is measured below 0.98,  $\Delta PF_y$  is computed by using  $|PF_{yphx} - 1|$ , where  $PF_{yphx}$  is the power factor of the severe phase at the PCC. The fuzzy control uses  $\Delta PF_y$  in the fuzzy system to create one output ( $\Delta I_q$ ) as the instruction to the bi-directional inverter. The instruction  $I_q$  is used to manipulate the reactive power flow of the energy storage system in order to improve the power factor of the network.

## Experimental Result and Discussion:

### Case Study 1: Impacts of high PV power output on the experimental LV distribution network

The objective of this case study is to investigate the impact of the intermittent PV power output on the experimental network. A constant load of 700 W and a 3.6 kW<sub>p</sub> PV system are connected at phase A of the experimental network. Figure 3 shows the load profile, PV power output and the power factor of the experimental case study. Figure 4 shows the voltage and VUF at the PCC. Initially, the PV system is generating 800 W which is slightly greater than the 700 W load. The VUF is recorded at 1% while the voltage is approximately 243 V. At 2:45PM, the PV power output starts to increase causing the system voltage to rise above 251V and the VUF is recorded at 3.4%. It is noticed that the power factor is fluctuating all the time. This is due to the intermittent PV power output. This condition might be happened in residential area during mid of the day where high PV power output and low load demand is occurred.

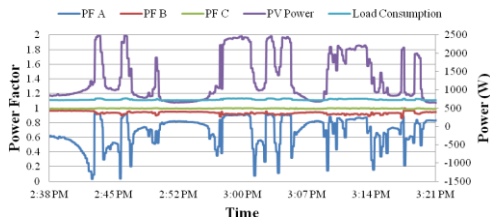


Figure 3: PV power output at Phase A, load at Phase A and power factor of all three phases of the experimental case study 1

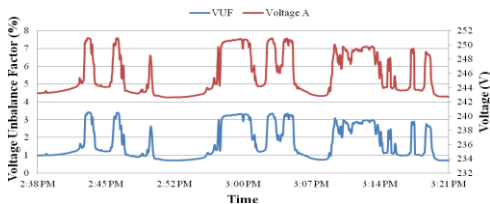


Figure 4: VUF and voltage at phase A of the experimental case study 1

### Case Study 2: Effect of using fuzzy logic controlled energy storage when PV is integrated.

This case study is designed to study the response of the fuzzy controlled energy storage system with respect to the changes of PV power output under a balanced load condition. A fixed load of 400 W is introduced to every phase. A 3.6 kW<sub>p</sub> PV system is connected to phase B of the network. Figure 5 shows the increment of PV power output has affects the three-phase voltages at 3.38pm. Due to the coupling effect, voltage at phase C dropped to 230 V although phase B has an excess power. The fuzzy control system detects the sudden change and instructs the bi-directional inverter to absorb the excess power generated by the PV system at phase B. The three phase voltages are restored to its nominal once the excess power is stored into the energy storage system. At

3.45pm, the control algorithm detects the voltage at phase C is out of range, therefore making an appropriate corrective action by adjusting the power flow of the energy storage system. Figure 6 shows the response of the energy storage system and the VUF of the experimental network. The VUF is recorded at 2% when the PV system generates excess power to the network. It is noticed that VUF is reduced to 0.5% when the energy storage system has performed to absorb the excess power from the network. Figure 7 shows the power factor is maintained at 0.98 by injecting appropriate amount of the reactive power to the network. At 3.38pm, it is noticed that there is a sudden drop in power factor, this is because the PV system starts to generate power to the network after synchronized with the experimental network.

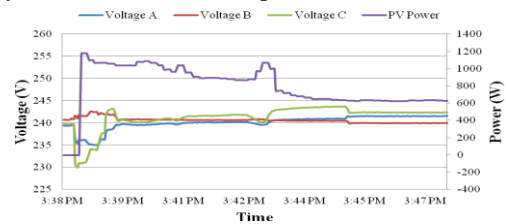


Figure 5: Three-phase voltages and PV power output of the experimental case study 2.

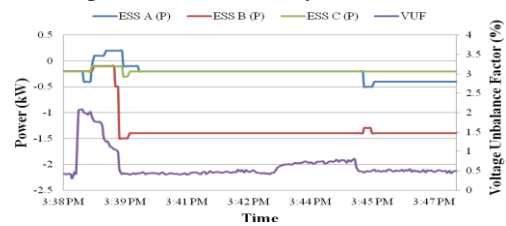


Figure 6: VUF and power output of the energy storage system of the experimental case study 2.

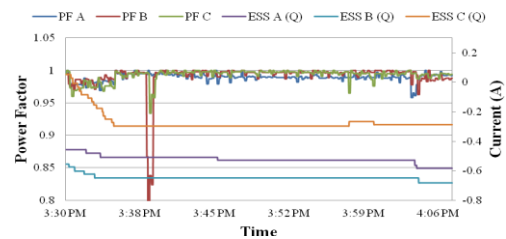


Figure 7: Power factor of all three phases and reactive power output of the energy storage system.

### Case Study 3: Effect of using energy storage when inductive load is connected.

This case study is used to investigate the effectiveness of the fuzzy controlled energy storage system to improve the power factor of the experimental network. In this experiment, a 2600 mH inductive load is connected to phase A. Figure 8 shows the VUF, voltage and its angle, power factor, reactive current control of the energy storage system and reactive power flow of the experimental network. It is noticed that VUF is reduced from 0.8% to 0.5% after the energy storage system supplies 192 Var to compensate the inductive load in the experimental network.

The fuzzy control algorithm is used to manipulate the amount of reactive current flow from the energy storage system to the network based on the network power factor. It is noticed that the power factor is maintained within 0.98 and unity power factor. Reactive power not only able to improve the power factor, it can also provide a support to the network voltage. Besides, the voltage angle also maintained at a degree of 120. This indicates that reactive power supplied by the energy storage system can improve power factor, VUF, voltage and voltage angle.

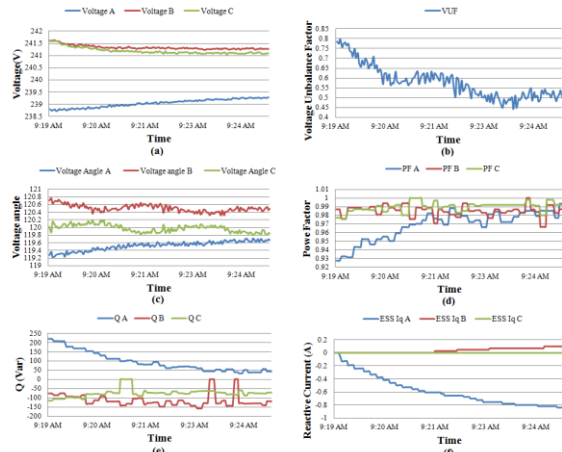


Figure 8: (a) Three-phase voltages, (b) VUF, (c) Voltage angle, (d) Power factor, (e) Reactive power flow and (f) Reactive current control of the energy storage system of the experimental case study 3.

#### Case study 4: Effect of using energy storage when electric car (EV) is connected to the network as load together with the PV integration.

This case study is designed to study the response of the proposed energy storage system to a sudden change in load demand with PV system. Figure 9 shows the VUF, EV power, PV power output and voltage at phase A. At 3.16pm, EV is charging at 2.4 kW causing the voltage at phase A to drop lower than 230 V. It is noticed that the fuzzy controller detects the sudden change and instruct energy storage system to inject power to the network. At 3.19pm, PV is connected to phase A of the network causing the voltage at phase A to increase. It is noticed that the fuzzy control algorithm is able to manipulate the power output of the energy storage system so to mitigate the VUF and voltage of the experimental network. At 3.25pm, the PV and EV are disconnected on a purpose and it is shown that the fuzzy controller is able to regulate the voltage and mitigate the VUF in a very short period.

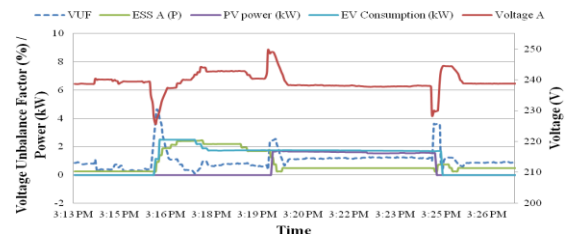


Figure 9: VUF, voltage, active power output of energy storage system, and PV power of the experimental case study 4.

#### Conclusion:

This paper presents a fuzzy controlled energy storage system to mitigate the VUF and voltage rise, improve power factor by manipulating the real and reactive power flow. Several scenarios under various generating and loading conditions are carried out to investigate the performance of the fuzzy controlled energy storage system. It is noticed that energy storage system that only allow real power control has limited capability. With the aid of reactive power in the distribution network, it can provide voltage support and also improve power factor issues caused by inductive loads. The experimental results show that the proposed fuzzy controlled energy storage system not only mitigate the voltage rise and VUF caused by intermittent PV power output, but also can improve the network power factor effectively.

#### References:

A. Jan von Appen, B. C. (2011). Assessment of the Economic Potential of Microgrids for Reactive Power Supply. *8th International Conference on Power Electronics - ECCE Asia*, (p. 8). The Shilla Jeju, Korea.

Canada, M. o. (2004). *Final Report on the August 14, 2003 Blackout in the United States and Canada: Causes and Recommendations*. Canada: U.S.-Canada Power System Outage Task Force.

Ferry A. Viawan, S. M. (July 2008). Coordinated Voltage and Reactive Power Control in the presence of distributed generation. *Power and Energy Society General Meeting - Conversion and Delivery of Electrical Energy in the 21st Century, 2008 IEEE* (pp. 1-6). Pittsburgh, PA: IEEE.

Prakash K. Ray, S. R. (2013). Classification of Power Quality Disturbances Due to Environmental Characteristics in Distributed Generation System. *Sustainable Energy, IEEE Transactions on (Volume:4, Issue: 2)*, 302 - 313.

Roberto Caldon, M. C. (2012). Voltage Unbalance Compensation In LV Networks With Inverter Interfaced Distributed Energy Resources. *2nd IEEE ENERGYCON Conference & Exhibition / Future Energy Grids and Systems Symp*, (pp. 527-532). University of Padova, Italy.

Wong, J., Lim, Y. S., & Morris, a. E. (2014). Novel Fuzzy Controlled Energy Storage for Low-Voltage Distribution Networks with Photovoltaic Systems under Highly Cloudy Conditions. *ASCE Journal of Energy Engineering*, 17.

# Effect of Glass Thickness on the performance of The ET200 Solar thermal Collector

N. Ihaddadene,<sup>1</sup> R. Ihaddadene,<sup>1</sup> A. Betka<sup>1</sup>

<sup>1</sup>University of M'Sila, Department of Mechanics, M'Sila, Algeria

**Abstract:** Solar energy available across the globe, obviously at different intensity, is a clean, sustainable and inexhaustible energy. It is the alternative to conventional energy sources. Solar thermal panels, called solar thermal collectors, convert solar radiation into heat recovered and used in the form of hot water. Several studies have been devoted to ameliorate the performance of solar water heating systems (Ihaddadene *et al.* 2014, Ihaddadene *et al.* 2014, Hazami *et al.* 2005). This paper aimed to study glass thickness effect of a solar collector on its efficiency. Experiments were performed on an active solar energy demonstration system (ET 200), illuminated with a halogen lamp. This former consists of water storage tank, a flat plate solar collector, a high-power lamp and a control and command cabinet. The flat plate solar collector consists of essentially four major components fabricated as a 'sandwich'; the glazing, air gap and insulation layers act to prevent heat loss from the solar collector to the environment, while the absorber plate coupled with the heat transfer tubes actively remove heat from the solar collector to water storage tank (see Figure1).



Figure 1 Experimental device.

Commercial glass panes having the same properties but with different thicknesses (3mm, 5mm, 6mm, and 8mm) were used. Trials were done at a fixed water flow rate of 5.9 l/h, taking the whole surface of the collector maintained at an horizontal position. The instantaneous efficiency of a solar collector is defined as the ratio of the useful flux extracted from water collector to the incident flux intercepted by glass collector.

Glass thickness acts as a thermal resistance to heat transfer from the halogen lamp to water flowing through the absorber in the solar collector and then to water tank. (see Figure2 and Figure3).

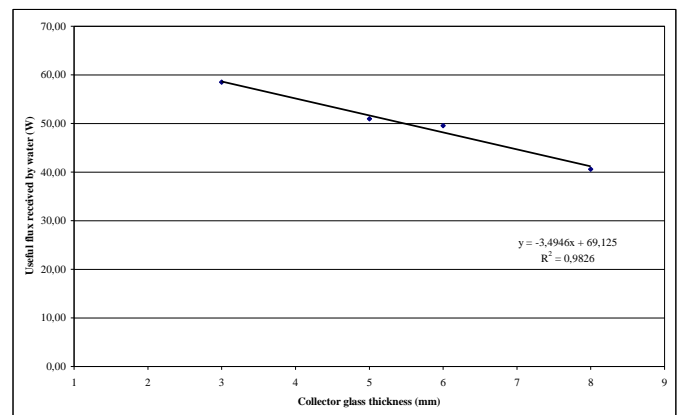


Figure 2 Effect of collector glass thickness on the effective power transmitted to water flowing through the solar collector.

As seen in Figure2, the useful power transmitted to water decreases linearly with the glass thickness according to the following mathematical relationship:  $E_u = - 3.495 \times e + 69.125$  ( $R^2=0.9826$ ).

Where,

$E_u$ : Useful flux received by water in watt (W),  
 $e$ : Collector glass thickness in millimeter (mm).

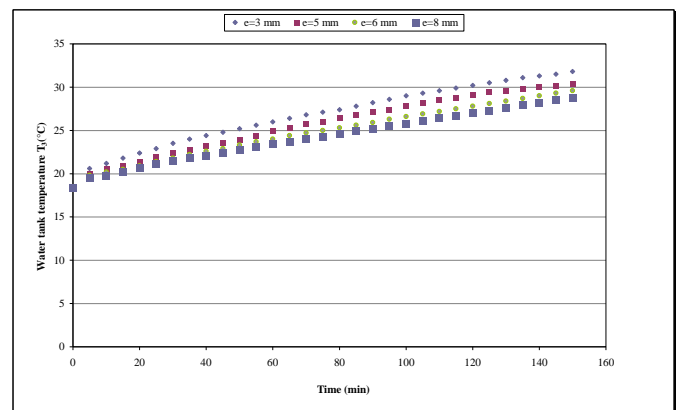


Figure 3 Effect of collector glass thickness on the evolution of water tank temperature.

As shown in Figure3 water tank is well heated when using the thinnest glass. The opposite result is obtained for the thickest glass.

The results showed that radiation intensity received by the glazed surface of the solar collector increases linearly with its thickness (see Figure4) according to the empirical relationship:

$$G = 0.0243 \times e + 0.6567 \quad (R^2 = 0.9324)$$

where,

G: Illuminance, i.e. incident solar flux by glass surface in kilowatt par square meter (kW/m<sup>2</sup>);

e: Glazing thickness of the solar collector in millimeter (mm).

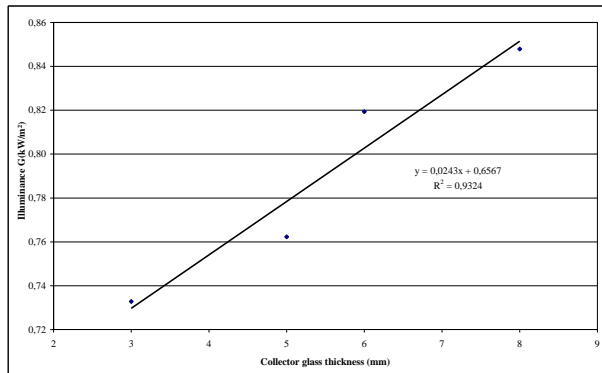


Figure 4 Effect of the glass thickness on the evolution of the illuminance G.

This result is due to the distance separating the collector surface and the halogen lamp (heat source); indeed, when the receiving surface approximates the heat source, it receives more heat energy, this is what happened in this experiment.

Glass thickness of the solar collector has a negative effect on the performance of ET 200 Solar collector (Figure5).

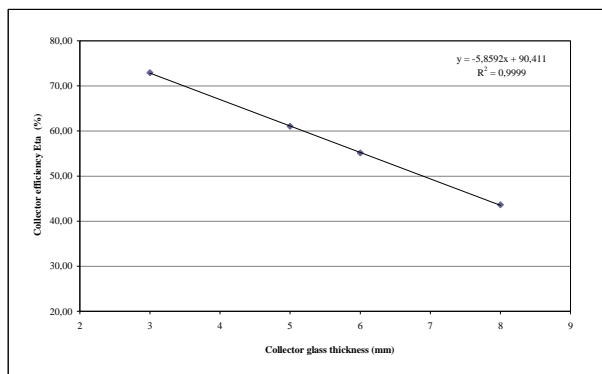


Figure 5: Effect of collector glass thickness on its efficiency.

It is observed that the lower value of the performance of the solar collector is recorded for the thickest glass (about 44%), in contrast to the thinner glass where this value is the highest one (in the order of 73%).

As illustrated in Figure5 the performance of the thermal collector decreases with the thickness of its glazing surface according to the following empirical relationship:

$$\eta = -5.86 \times e + 90.41 \quad (R^2 = 0.99)$$

Where,

$\eta$ , Solar collector performance in steady state expressed in percentage (%);

e, Solar collector glass thickness in millimeters (mm).

This result is in agreement with the energy carried by water and transmitted to water tank.

It is necessary to use thin glass to improve the efficiency of the cited apparatus.

Keywords: solar energy, solar collector efficiency, glass thickness, radiation intensity.

### References:

Ihaddadene, N., Ihaddadene, R., Mahdi, A. (2014) . Effects of double glazing on the performance of a Solar thermal collector. *Appl. Mech. Mater. J.*, 492, 118-122.

Ihaddadene R., Ihaddadene N., Bey M., Hamidibacha F. Z. (2014), The effects of volumetric flow rate and inclination angle on the performance of a solar thermal collector, *Energ. Conver. Manage.*, 78, 931-937.

Hazami, M., Kooli, S., Lazaar, M., Farhat, A., Belghith, A.(2005), Performance of a solar storage collector, *Desalination*, 183,167-172.

# La variation de la température dans le sol à de faibles profondeurs dans la région de Noumerat à Ghardaïa

N. Chenini<sup>#1</sup>, S. Chabou-Mostefai<sup>\*2</sup>

<sup>#</sup> *Unité de Recherche Appliquée en Energies Renouvelables, URAER, Centre de Développement des Energies Renouvelables, CDER, 47133, Ghardaïa, Algeria*

*BP: 88 Gart Taam Z.I Bounoura Ghardaïa, Algérie*

<sup>1</sup>chenini\_nadir@uraer.dz

<sup>\*</sup> *Ecole Nationale polytechnique d'Alger*

*10 Avenue Hacen Badi El Harrach .BP 182 – Alger, Algérie*

<sup>2</sup>salima.chabou@g.enp.edu.dz

<sup>2</sup>salicha@yahoo.fr

**Résumé** – La présence d'eaux thermales dans la région de Ghardaïa, dont la température est 41.5 °C [1] en Zelfana et 40 °C [2] en Guerrara, nous a conduit à déterminer la variation de la température du sous-sol. Dans cette étude géothermique on s'intéresse aux premiers mètres en dessous de la surface du sol. Nous avons utilisé les données de températures du sol et les données des températures ambiantes journalières mesurées durant l'année 2013 représentatives de la station radiométrique installée dans l' Unité de Recherche Appliquée en Energies Renouvelables située à Noumerat (Ghardaïa), (latitude 32.36 °N, longitude 3.80 E et altitude 469 m). Le modèle utilisé est développé à partir de l'équation instationnaire de la chaleur pour un milieu homogène.

L'objectif de ce travail est la détermination des variations, durant une année, de la température du sol à de faibles profondeurs de la région de Noumerat pour une éventuelle utilisation énergétique.

**Mots clés**- Géothermique, température, Ghardaïa, station radiométrique, faibles profondeurs.

## Introduction

La région d'étude se situe dans le Sud algérien, au centre du Sahara septentrional. Elle renferme d'importantes réserves d'eaux souterraines dont les deux principales nappes sont: la nappe du Continental Intercalaire et la nappe du complexe terminal du Sahara septentrional. Ces eaux souterraines jouent un rôle très important en géothermie. Cette énergie géothermique possède de multiples utilisations (chauffage urbain, pisciculture et électricité)

La température de l'air ambiant, le type de sol, la présence et la circulation d'eau, la couverture du sol et la profondeur ont tous une influence sur la température du sol dans les premiers mètres. Pour les faibles profondeurs, la température du sol varie de manière significative le long de l'année avec la profondeur [3].

Le flux géothermique est exprimé en  $w/m^2$ . Sa moyenne mondiale est l'ordre de  $0.06 w/m^2$ . Ce

flux de chaleur est plus de 1000 fois inférieur à celui apporté par le soleil sur la Terre et est donc difficilement exploitable directement [3].

## METHODOLOGIE

Nous avons choisi pour cette étude la région de Noumerat située à 15 km au Sud-Est de Ghardaïa pour les données de la station radiométrique installée dans l'Unité de Recherche Appliquée en Energies Renouvelables et de la température du sol en surface fournie par des données satellite de la NASA via le logiciel RETScreen Plus [4]. Notre objectif est la détermination des variations, le long de l'année, de la température du sol à de faibles profondeurs de la région de Noumerat.

La wilaya de Ghardaïa se situe au Centre du Sahara Septentrional, elle est limitée (figure 1): au Nord par les wilayas de Laghouat et de Djelfa, au Sud par la wilaya de Tamanrasset, à l'Est par la wilaya d'Ouargla, à l'Ouest par les wilayas d'Adrar et d'El-Bayadh.

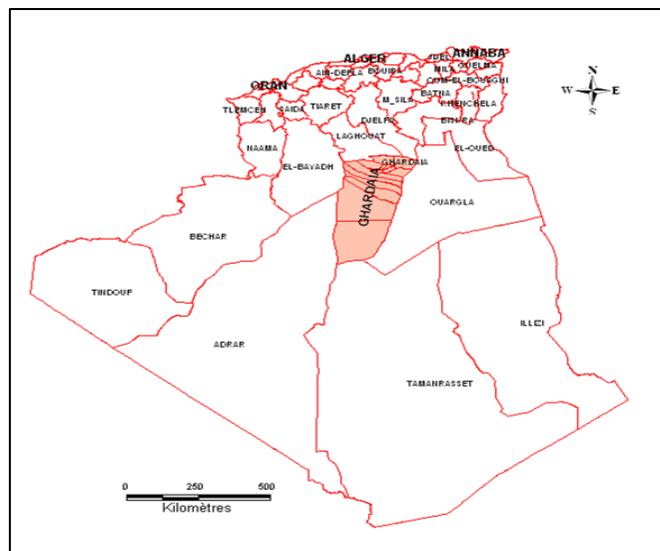


Fig.1 Situation géographique de la région d'étude.

### A. Aspect climatique:

Le climat de la région de Ghardaïa est Saharien. Il se caractérise par une saison chaude et sèche (Mai à Septembre) et une autre froide (Novembre à la mi-Avril) et une période tempérée (Octobre et la deuxième quinzaine d'Avril). Notons une grande différence entre les températures moyennes de l'été et de l'hiver (plus de 20 °C). La moyenne annuelle est de 22,6°C (figure 2).

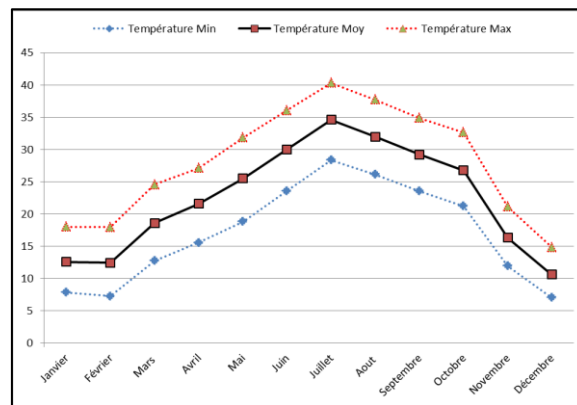


Fig.2 Variations mensuelles de la température.

Les valeurs de la température enregistrée caractérisent un climat saharien. En 2013 le maximum du mois le plus chaud est de 40,3°C en juillet, et le minimum le plus froid est de 7,0 °C en février.

#### B. Aspect géologique et hydrogéologique:

La détermination de la température du sous-sol en profondeur nécessite la connaissance de la nature de ce dernier.

Du point de vue géologique, la région de Ghardaïa est située aux bordures occidentales du bassin sédimentaire secondaire du Sahara, sur un grand plateau subhorizontal de massifs calcaires d'âge Turonien appelé couramment " la dorsale du M'Zab". L'épaisseur de ces massifs calcaires recoupés par les sondages est de l'ordre de 110 mètres.

Sous les calcaires turoniens on recoupe une couche imperméable de 220 mètres formée d'argile verte et de marne riche en gypse et en anhydrite; elle est attribuée au Cénomaniens. L'étage de l'Albien est représenté par une masse importante de sables fins de grès et d'argiles vertes. Elle abrite des ressources hydrauliques importantes avec une épaisseur de l'ordre de 300 mètres.

Les alluvions quaternaires formées de sables, galets et argiles tapissent le fond des vallées des oueds de la dorsale sur 20 à 35 mètres d'épaisseur.

Du point de vue hydrogéologique, la région d'étude englobe une série de couches aquifères qui ont été regroupées en deux réservoirs appelés le Continental Intercalaire (nappe de l'Albien) et le Complexe Terminal (figure 3).

La nappe du Continental Intercalaire draine, d'une façon générale, les formations gréseuses et grès-argileuses du Barrémien et de l'Albien. Elle est exploitée, selon la région, à une profondeur allant de 250 à 1000 m. L'alimentation de cette nappe bien qu'elle soit minime, provient directement des eaux de pluie au piémont de l'Atlas Saharien au niveau de l'accident Sud-Atlasique [5].

En fonction de l'altitude de la zone d'étude et de la variation de l'épaisseur des formations postérieures au Continental Intercalaire la nappe est jaillissante et admet des pressions en tête d'ouvrage de captage (Zelfana, Guerrara et certaines régions d'El Menia) elle est aussi exploitée par pompage à des profondeurs importantes, dépassant parfois 120m (Ghardaïa, Metlili, Berriane et certaines régions d'El Menia).

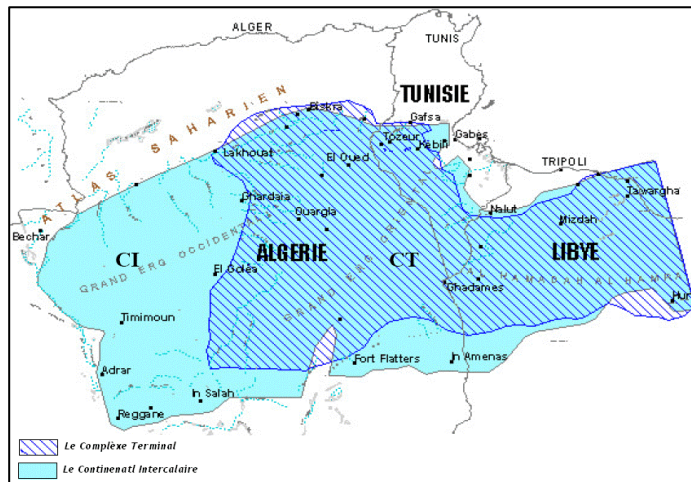


Fig.3 Situation géographique des deux nappes aquifères le Continental Intercalaire et le Complexe Terminal [6].

**Problématique :**

En l'absence de données de température du sous-sol pour la région de Ghardaïa, nous avons utilisé la température de l'air ambiant et la température du sol en surface de la région d'étude afin de représenter la variation de la température du sous-sol à de faibles profondeurs. On établit à l'aide du logiciel OriginPro 8 les figures 4 et 5 qui montrent que le signal des deux températures a une forme sinusoïdale.

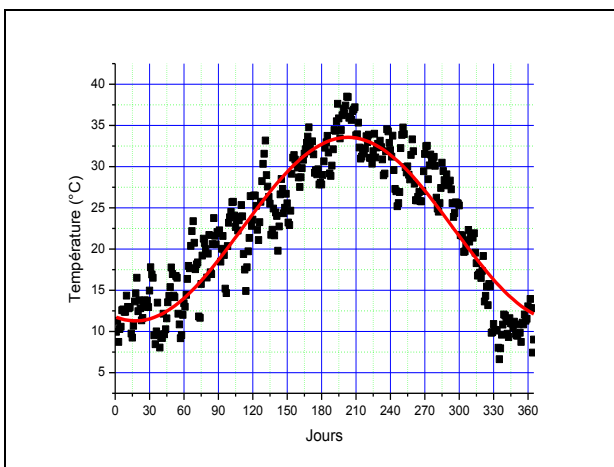


Fig.4 Evolution de la température ambiante (°C) mesurée sur une année et son lissage en fonction sinus.

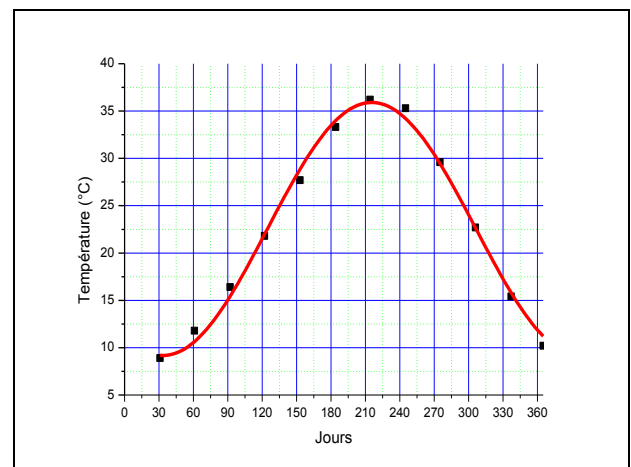


Fig.5 Evolution de la température du sol (°C) sur une année et son lissage en fonction sinus.

## RESULTAT ET DISCUSION

On a considéré la température ambiante journalière durant une année représentative de la zone d'étude, afin de faciliter l'emploi de ces données horaires de température, lors des calculs ultérieurs, l'évolution de la température en fonction du temps (jours) a été représentée adéquatement par des fonctions sinus (figure 4) :

$$T(t) = T_{\text{moy}} + A \sin(\omega(t - t_0)) \dots\dots\dots (1) \text{ où}$$

$\omega$  : Fréquence angulaire égale à 0,0172 rad/jour, ce qui correspond à une période de 365 jours.

$T_{\text{moy}}$  : Température moyenne annuelle.

$A$  : Amplitude de la variation de température.

$t_0$  : Jour de l'année où la température moyenne est atteinte.

En effet pour  $t = t_0$  :  $\sin(\omega(t - t_0)) = 0$  et  $T = T_{\text{moy}}$

Ces trois derniers paramètres ( $T_{\text{moy}}$ ,  $A$  et  $t_0$ ) sont obtenus par lissage des données.

Après le lissage des données de la température du sol à la surface et la température de l'air ambiant, nous avons établi la figure ci-dessous :

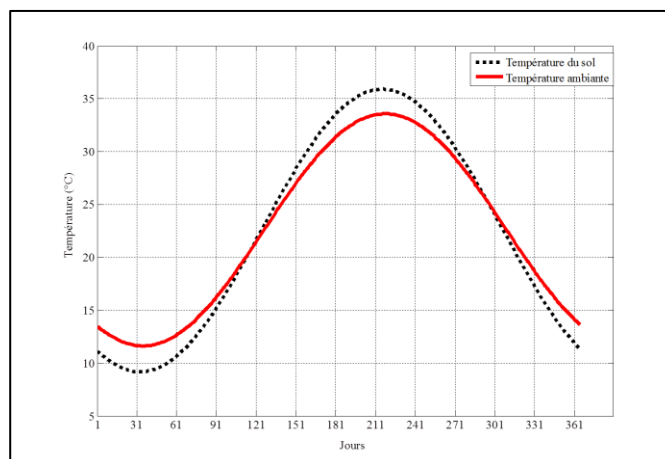


Fig.6 Evolution des deux températures ambiantes et de surface du sol après leur lissage en fonction sinus.

Dans cette figure, on voit que la température du sol à la surface prend la valeur la plus élevée en Eté et la plus basse en Hiver par rapport à la température de l'air, cela est du à l'inertie thermique du sol. En saison chaude, la durée entre le lever et le coucher du soleil est plus grande pour les rayons reçus au sol (14 heures et 08 minutes) l'irradiation reçue est de  $8378 \text{ Wh/m}^2$  pour le mois de Juin et en saison froide la durée est plus courte 09 heures et 53 minutes, l'irradiation reçue est de  $3255 \text{ Wh/m}^2$  pour le mois de Décembre. Ce phénomène constaté sur le cycle jour-nuit est encore plus marqué sur le cycle des saisons, à l'arrivée du printemps puis de l'été, le sol va progressivement accumuler la chaleur apportée par le soleil en la captant, ce qui ralentit la montée des températures. Le phénomène inverse se produit en automne puis en hiver : le sol va accumuler le froid en restituant la chaleur qu'il aura stockée durant l'été, ce qui ralentit la baisse des températures.

En géothermie de surface, on s'intéresse aux premiers mètres en dessous de la surface du sol. De ce point de vue, le sol est assimilé à un massif semi-infini homogène et le problème supposé

monodimensionnel, le mode de transfert de chaleur dominant est la conduction. L'équation instationnaire de la chaleur dans ce cas s'écrit:

$$\frac{\partial T}{\partial t} = Df * \frac{\partial^2 T}{\partial z^2} \dots \dots \dots (2)$$

Où

T : Température du sol, fonction de t et de z (°C).

t : Temps (s).

z : Profondeur en dessous de la surface du sol (m).

Df : Diffusivité thermique (m<sup>2</sup>/s).

Pour résoudre cette équation différentielle {Eq. (2)}, on a besoin de prescrire des conditions initiales et aux limites introduites ci-dessus. Cela donne la distribution spatio-temporelle suivante de la température du sol:

$$T(z,t) = T_{moy} + A * \exp(-z / d) * \sin(\omega(t - t_0) - z / d) \dots \dots \dots (3)$$

Où:

d : représente la profondeur de pénétration (m) de l'onde de chaleur dans le sol. Elle est donnée par:

$$d = \sqrt{\frac{2 Df}{\omega}}$$

Pour calculer la valeur de la diffusivité thermique on utilise les données C<sub>p</sub>, λ, ρ adaptée à la région.

Le sol de la région d'étude est un massif calcaire d'âge Turonien puissant de l'ordre de 110 mètres, où:

- La conductivité thermique λ= 2,3 W·m<sup>-1</sup>·K<sup>-1</sup> [7]
- La capacité thermique massique C<sub>p</sub> = 1000 J.kg<sup>-1</sup>·K<sup>-1</sup> [7]
- La densité ρ = 2740 kg.m<sup>-3</sup> [8]

La relation s'écrit : d<sub>(calcaire)</sub> = 2,9 m et Df<sub>(calcaire)</sub>=8,39\*10<sup>-7</sup> m<sup>2</sup>/s

On établit une figure (fig.7) qui montre la variation de la profondeur de pénétration de l'onde de la chaleur dans le sol en fonction des différentes périodes (jour, semaine, mois, année).

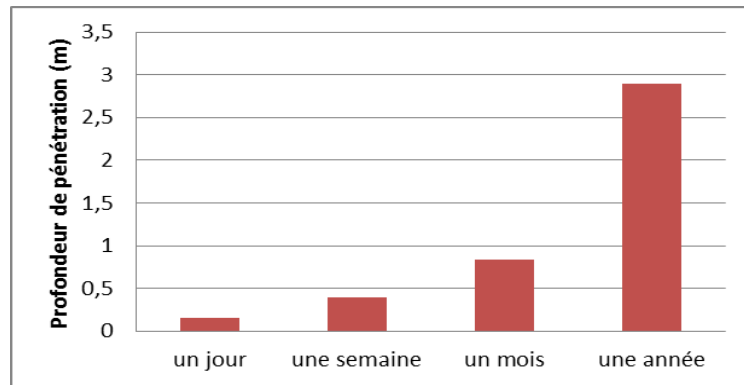


Fig.7 profondeur de pénétration thermique dans la région de Noumerat en différentes périodes.

D'après l'équation (3), on établit les figures ci-dessous qui représentent l'évolution de la température du sous-sol à faible profondeur et pour une année (figure 8), et pour les quatre saisons (figure 9).

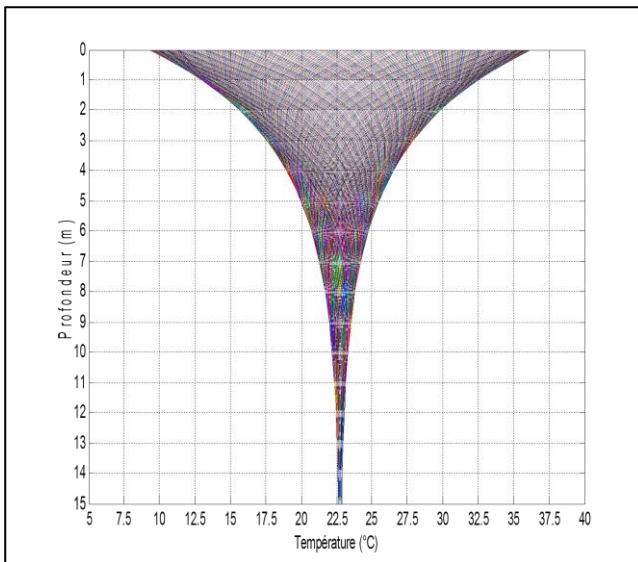


Fig.8 Variation de la température en fonction du temps et de profondeur dans la région d'étude.

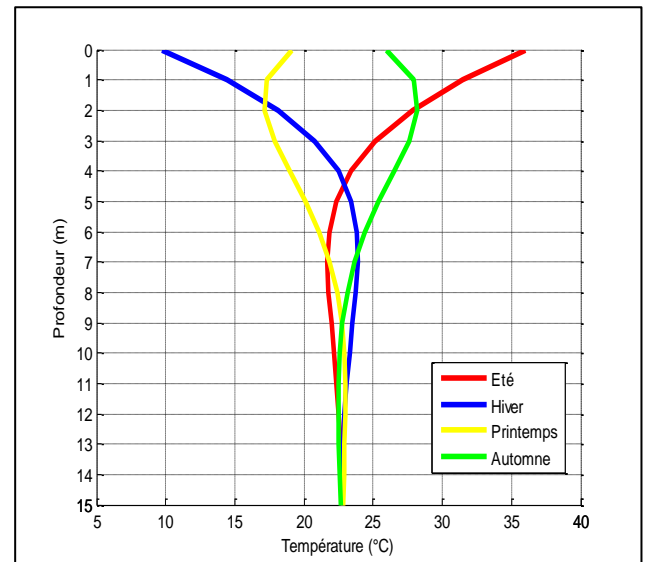


Fig.9 Evolution de la température du sous-sol en fonction des saisons.

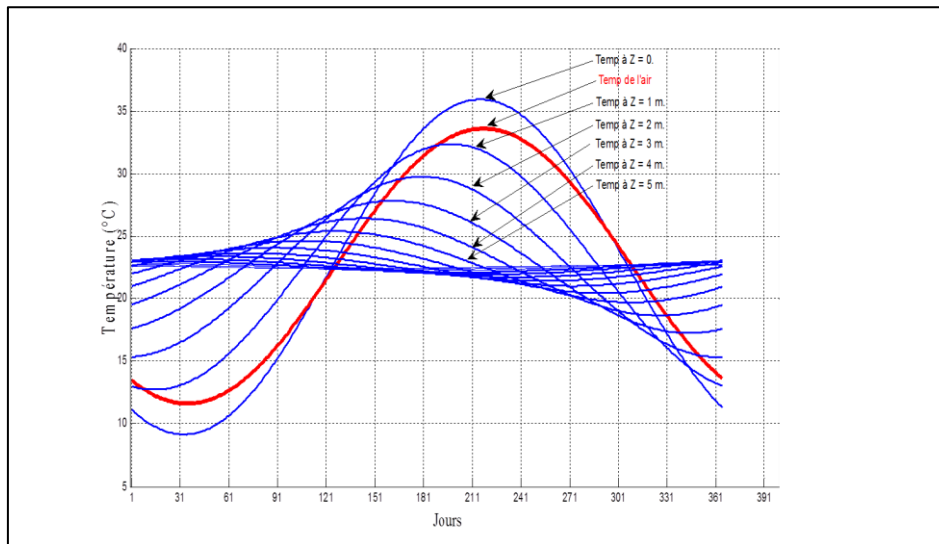


Fig.10 Evolution de la température dans le sol pour les différentes profondeurs.

Dans cette figure, on observe qu'à 3 mètres de profondeur la fluctuation de la température est entre 17,82 °C et 27,82 °C pour toutes les saisons de l'année avec une différence de 10 °C. Aussi, à 4 mètres de profondeur la fluctuation de la température est de 20,45 °C à 24,62 °C pour toutes les saisons de l'année avec une différence de 4,17 °C. Au-delà d'une profondeur de quatre fois la profondeur de pénétration (d), la température du sol est sensiblement constante tout au long de l'année (fig.8 et 9), sa valeur est fonction du gradient géothermique local 2,7 °C par 100 m [9].

Nous pouvons avancer que l'amplitude du signal de la température décroît quand la profondeur augmente et au-delà d'une distance égalant quatre fois la profondeur de pénétration, la température du sol se stabilise aux alentours de la température moyenne annuelle du sol en surface.

Aussi, le signal de la température du sous-sol est déphasé par rapport à la surface d'une valeur :  $\Delta t = -z/\omega d$ .

## CONCLUSION:

Pour étudier la variation de la température du sol en profondeur, on tient compte de la nature du sol et du climat du milieu à étudier avec la température de l'air et la température du sol en surface.

Cette étude montre que les variations saisonnières sont amorties dans les premiers mètres et que la température du proche sous-sol tout au long de l'année est égale à la moyenne des températures annuelles. Au-delà d'une profondeur de quatre fois la profondeur de pénétration (d), c'est le gradient géothermique qui contrôle la température.

## Références bibliographiques:

[1] M. Gautier et N.Gousskov, 1952, 'LE FORAGE DE ZELFANA, sondage de reconnaissance et d'étude de la nappe Albienne au Sahara', Extrait de 'TERRES ET EAUX', n° 4, 3<sup>ème</sup> trimestre 1948.

[2] M. Gautier et N.Gousskov, 1952, 'LE FORAGE DE GUERRARA, Deuxième sondage d'étude et premier grand sondage d'exploitation de la nappe Albienne au Sahara', Extrait de 'TERRES ET

EAUX', n° 13, 1er trimestre 1951.

[3] J. Lemale, 'La géothermie', 2<sup>ème</sup> édition, Dunod/Le Moniteur, collection Technique et ingénierie, janvier 2012, 320 pages, ISBN 978-2-10-057238-0.

[4] [http://www.retscreen.net/fr/d\\_data\\_w.php](http://www.retscreen.net/fr/d_data_w.php).

[5] A.N.R.H Secteur de Ghardaïa, décembre 2011, 'Inventaire des forages d'eau et enquête sur les débits extraits de la wilaya de Ghardaïa', rapport final de l'exercice 2011, 88 pages.

[6] Système Aquifère du Sahara Septentrional (Algérie, Tunisie, Lybie) : Gestion commune d'un bassin transfrontière/ OSS. Collection synthèse n°1 : Tunis, 2008, 48 pages.

[7] M. HAMDANI, 2011, 'Etude et Effet de l'Orientation de deux Pièces d'un Habitat en Pierre Situé à Ghardaïa', Mémoire de Magister, Université Abou-Bakr Belkaïd – Tlemcen.

[8] Office National de Recherche Géologique et Minière, 1999, ' Livret des substances utiles non métalliques de l'Algérie, Wilaya de Ghardaïa', Boumerdes.

[9] D. Takherist et L. Hamdi, 1995, 'Anomalie Thermique de In-Salah: Conséquences Possibles sur le Potentiel Pétrolier', Contribution de SONATRACH Division Exploration, 19 pages.

# Optimizing a Sustainable Desalination System in Saudi Arabia: A Comparison between PV-RO and CSP-MED

Noura Y. Mansouri and Ahmed F. Ghoniem

Mechanical Engineering, Massachusetts Institute of Technology, Cambridge, MA, USA

## ABSTRACT

Water scarcity is a global crisis; the MENA region is one of the most water-stressed regions. Saudi Arabia currently burns approximately 1.5 million barrels of crude oil equivalent daily to produce water, through desalination, and for electricity generation [1]. If business-as-usual continues, it is expected that Saudi Arabia will burn over 8 million barrels per day of crude oil equivalent by 2040 [1] for the same purposes.

Solar irradiance is favourable in the MENA countries as it receives approximately %22-26 of the total solar irradiance reaching Earth's land [1]. Saudi Arabia's DNI is classified in the range between 2001-2600 kWh/m<sup>2</sup>/y [1]. Indeed, the Empty Quarter desert is believed to receive enough solar radiation to power two Earths. This abundant resource makes it only natural to consider utilizing solar energy for various applications.

Per capita renewable water in Saudi Arabia is about 200-500 m<sup>3</sup>/cap/year and is expected to be under 200 m<sup>3</sup>/cap/year between 2020-2030, that is much below the threshold for water poverty, which is at 1000 m<sup>3</sup>/cap/year [1].

Freshwater demand in MENA countries is escalating and is expected to grow fivefold over the next five decades. Half of the global desalination capacity is already done in MENA which reached 9.2 Bm<sup>3</sup>/y in 2010 [1]. Saudi Arabia's water shortages are expected to increase by 20–40 km<sup>3</sup> yearly. Similarly, electricity demand is also escalating in these countries and with the forecast of water desalination demand, this is expected to escalate further [1].

There are many drivers for Saudi Arabia to launch solar-desalination projects, this includes [ [1] [2]]: water demand, financial strength, experience with existing desalination facilities, climate change mitigation and adaptation efforts, reducing carbon emissions, escalating local energy demands and therefore limited availability of fossil fuels, and the political will to introduce solar to energy mix at 10% by 2020, 20% by 2030 [3].

Coupling desalination with renewable energy sources has a great potential in MENA, this is particularly a necessity in Saudi Arabia given all the challenges tied with escalating energy demand, water demand, water scarcity, escalating carbon dioxide emission and virtually unlimited solar irradiance. Saudi Arabia has the largest CSP desalination potential, estimated at 23.7 Bm<sup>3</sup>/y. Therefore, for Saudi

Arabia, CSP-powered seawater desalination could be the way forward [1].

The King Abdullah Initiative for Solar Desalination has launched plans to utilize solar energy in desalination plants. Starting with a capacity of 30,000 m<sup>3</sup>/day to meet water demands of Al Khafji using PV-RO in the first phase, and building up to 300,000 m<sup>3</sup>/day in the second phase, with the aim to reach 100% solar desalination of the entire plants by 2019.

This work looks at the matchmaking between the water desalination system and the solar power system, and compares the two designs of PV-RO and CSP-MED to optimize a design for Al Khafji.

## Keywords

Seawater desalination, solar desalination, sustainable desalination, PV-RO, CSP-MED, Saudi Arabia.

## 1. INTRODUCTION

Saudi Arabia is a desert country with a harsh dry weather, with no permanent water bodies and very limited rainfall, estimated at around 30-550 mm per year [4]. It is located in a water-stressed MENA region and ranks as a country with absolute water scarcity [5] as its renewable water per inhabitant ratio is much lower than the threshold for water poverty, which is at 1000 m<sup>3</sup> per capita per year [6]. Therefore, Saudi Arabia relies heavily on desalination to meet the growing water demands, and the entire process is highly subsidized by the government, from production, to transport to distribution. In fact, water tariffs in Saudi Arabia are among the lowest in the world ranging from US\$0.06 to US\$0.10/m<sup>3</sup> [7], and sometimes even reaching as low as US\$0.05 (Jeddah) and US\$0.03 (Riyadh) [8]. This, of course, is a great disincentive for water conservation in the country.

The annual renewable freshwater resources is equivalent to 2.4 km<sup>3</sup>/yr while the abstraction of water for use is much more, at 22 km<sup>3</sup>/yr [9]. Water resources in the kingdom include renewable groundwater representing 11.7% of the groundwater reserves and non-renewable groundwater representing 88.3% of the groundwater reserves [5]. Saudi Arabia has pumped up most of its non-renewable ground water due to the self-sufficiency food project which was initiated in the early Seventies for national security reasons. The excessive pumping of underground water has been used to irrigate part of the desert for the production of wheat [10].

It is estimated that between years 1970 up to 2012, around 21 km<sup>3</sup> has been pumped on a daily basis [11]. The desert was being irrigated with water to produce wheat that far exceeds local consumption and therefore nearly half of the production was exported to international markets. In year 2006 Saudi Arabia was the 6<sup>th</sup> largest exporter of wheat [10, 12]. Despite efforts to halt the self-sufficiency food project to reduce agricultural demands for water, demand is still set to rise and is expected to double by 2025.

The total installed capacity of water desalination in Saudi Arabia of nearly 2,922,436 m<sup>3</sup>/day [8], the technology used is primarily RO, 46.8%, followed by MSF, 43.2%, followed by MED, 9.1%, ED, 0.9%, and others. Most of the demand comes from municipal uses, 74.7%, followed by industrial 20.7%. Desalinated water comes from seawater, 76.8%, then brackish water, 22.1%. All the desalination systems use fossil fuels, and plans are underway to utilize the limitless solar resource through the King Abdullah Initiative for Solar Desalination. Starting with Al Khafji, which is located at the border between Saudi Arabia and Kuwait, of what was previously known as the Saudi-Kuwait neutral zone. It has come to existence after the discovery of Al-Khafji oil field in 1960. Located in Latitude (N) 28.50671 and Longitude (E) 48.45504, Al-Khafji is inhabited by a population of 60,414 and a density of 7.15 people/km<sup>2</sup>. The proposed design for Al Khafji by the initiative is to use a PV-RO. This paper will propose an alternative design with different sets of advantages.

## 2. SOLAR-DESALINATION TECHNOLOGY OPTIONS

### 2.1 Desalination Technology Options

Generally, there are two types of desalination technologies, (i) desalination using membrane separation, and (ii) desalination using thermal evaporation. Of the many desalination technologies, the most deployed technologies around the world are mainly RO, 59.85%, MSF, 25.99%, MED, 8.20%, and ED, 3.53%, using oil and natural gas fuels as a source of energy [13]. A brief technical overview on the three leading desalination technologies, using [14] [13]:

#### 2.1.1 Reverse Osmosis (RO)

RO is a mechanical membrane separation process that recovers water from a saline solution pressurized to a point greater than the osmotic pressure of the solution. Membrane filters hold back the salt ions from the pressurized solution, allowing only water to pass. RO membranes are sensitive to pH, oxidizers, organics, algae, bacteria, particulates and fouling. Pre-treatment is an important step and it contributes to the cost and energy consumption

Recently, micro-, ultra-, and nano-filtration has been proposed as an alternative to the chemical pre-treatment of raw water in order to avoid contamination of the seawater by the additives in the surrounding of the plants.

Post-treatment includes removing dissolved gases (CO<sub>2</sub>), and stabilizing the pH via the addition of Ca or Na salts, and removing dangerous substances. RO technologies are characterized by:

- No (heat/thermal) energy required
- Typical electricity consumption: 2.5-7 kWh/m<sup>3</sup>

- Energy consumption is a function of water salinity
- Water quality: 200-500 ppm
- Capacity: <20,000 m<sup>3</sup>/d

#### 2.1.2 Multi-Stage Flash (MSF)

MSF is a thermal distillation process. It involves, evaporation and condensation. The incoming feed water runs through the tubes at the upper section of the stages and is heated to maximum temperature (top brine temperature). The hot water enters the first stage and this sudden introduction into the chamber with lower pressure causes it to boil very quickly and “flashes” into steam. Vapor generated is condensed around the tubes of heat exchangers and is collected in each stage as fresh water. Tubes are cooled by incoming feed water. The process is repeated 20-40 times. MSF is widely used in the Middle East (Saudi Arabia, UAE and Kuwait).

The system is very robust – especially suited when the quality of the feed water is unfavorable (high salinity, temperature and contamination). MSF technologies are characterized by:

- Typical heat requirement: 250-330 kJ/kg
- Typical electricity consumption: 3-5 kWh/m<sup>3</sup>
- Water quality: < 10 ppm
- Capacity: <76,000 m<sup>3</sup>/d

#### 2.1.3 Multi-Effect Distillation (MED)

MED is a thermal distillation process. The feed water is sprayed onto the evaporator surface of different chambers (effects) in a thin film to promote evaporation after it has been preheated in the upper section of each chamber. The evaporator tubes in the first effect are heated by steam extracted from a power cycle or from a boiler. The first effect is condensed inside the evaporator tubes of the next effect, where again vapor is produced. The surfaces of all the other effects are heated by the steam produced in each preceding effect. Each effect must have a lower pressure than the preceding one. This process is repeated up to 16 effects. The steam produced in the final effect is condensed in a separate heat exchanger “the final condenser,” which is cooled by the incoming seawater, which is then used as preheated feed water for the desalination process. MED technologies are characterized by:

- Typical heat consumption: 190-390 kJ/kg
- Process steam at less than 0.35 bar
- Typical electricity consumption: 1.5-2.5 kWh/m<sup>3</sup> (pumping and control)
- Water quality: < 10 ppm
- Capacity: <36,000 m<sup>3</sup>/d

The following two tables present different ranges of energy use and costs for desalination systems cited in the literature, Miller [15] reviews energy use for desalination and explains the different types of energy involved, heat and electricity. He explains that due to the fact that RO’s energy use and cost is correlated to salinity, seawater RO (SWRO) and brackish water RO (BWRO) are made separate.

**Table 2-1 Energy Use for Desalination (kJ/kg)**

Ref.	MSF	MED	VC	SWRO	BWRO
[16]	230			27	
[17]	95-252	107-132	22-29		
[18]	216-288			18-22	11
[19]			22-58		
[20]				14	7.2

**Key:**

VC: Vapor Compression

SWRO: Seawater RO

BWRO: Brackish water RO

The figures for energy consumption in table 2-1 for MSF, MED and VC includes both thermal energy and electricity, whereas, that for SWRO and BWRO is for electricity.

**Table 2-2 Desalination Costs (\$/m3 fresh water)**

Ref.	MSF	MED	VC	SWRO	BWRO
[21]	1.10-1.50	0.45-85	0.87-0.92	0.45-0.92	0.20-0.35
[14]	0.70-0.75			0.45-0.85	0.25-0.60
[22]		1.35		1.06	
[23]	1.31-5.36			1.54-6.56	
[24]	0.80	0.45		0.72-0.93	

**2.2 Solar Technology Options**

The literature [25] [26] [27] provides a comprehensive overview of solar desalination. Coupling a solar system to a desalination system depends on many factors, including: plant size, feed water salinity, remoteness, availability of grid electricity, technical infrastructure and the type of solar technology available. [25]

There are few factors to consider when assessing a solar resource and choosing a technology. Satellites are used to measure the solar radiation from the top of the atmosphere before it passes through the ozone layer, air molecules, aerosols, clouds and water vapor [28]. It can be measured in different ways, most commonly: (i) direct normal irradiance (DNI), which comes in a straight line from the sun. DNI is highly sensitive to weather conditions from clean to hazy, sometimes 3-5 times more sensitive to aerosols (ground dust, sand storms, industrial pollution, urban pollution...etc) than GHI [29]; (ii) global horizontal irradiance (GHI), which is the total amount of shortwave radiation received by a surface horizontal to the ground, and it includes the DNI and the diffuse horizontal

irradiance (DIF), which does not arrive in a straight line but from different directions after being scattered by molecules and particles [28]. It is easier and more common to get GHI data as it only needs 2-3 years of measurements, whereas DNI takes up to 5-15 years [29].

**2.2.1 Photovoltaics (PV)**

Photovoltaic converts solar irradiance directly into direct current electricity. Photons from the sun break up the negative-positive pairs. Some electrons are knocked out towards the top layer and into the metal conductor strips, thus generating electricity. The electrons (negative particles) move in to fill the holes (positive particles), creating an electric field in the p-n junction.

The two most common categories of PV are: (i) Crystalline Wafer Silicon, projected to make up approximately 66% of world-wide production capacity in 2015; and (ii) Thin Film, projected to make up approximately 34% of world-wide production capacity in 2015. PV has a reduced efficiency with increased irradiance.

PV pertains to GHI, PV yields increase roughly linear to GHI [30], which is less variable and more precise to measure and easier to derive from satellites.

**2.2.2 Concentrated Solar Power (CSP)**

CSP is a thermal system that concentrates sunlight on a working liquid that transfers the heat to the brine water to vaporize it to produce energy.

The two most common types of CSP are: (i) Line-concentrating, such as (a) Parabolic Trough, and (b) Linear Fresnel, and (ii) Point-concentrating, such as (a) Solar Tower / Heliostats and (b) Dish Stirling.

CSP pertains to DNI. CSP systems require radiation that is direct so it can be focused. CSP yields roughly linear to DNI [30], which is affected by clouds, aerosols, high humidity, dust sandstorms, fog, etc.

If we compare CSP to PV in terms of providing base load with minimum intermittency, CSP reported much more stable performance than PV [6]. CSP has the compatibility for thermal energy storage compared to PV. In terms of land requirements, CSP typically requires a total area of 40,469 m<sup>2</sup> compared to a total area of 31,970 m<sup>2</sup> in PV [31].

**2.3 Optimizing a Solar-Desalination Design Desalination Technology Options**

To optimize a sustainable desalination system, matchmaking between a desalination system and a solar system is important. It involves the coupling between the output of energy from a solar system and the input of energy required by the desalination system, and comparing and understanding the differences and advantages for a specific site location. The following table summarizes the differences between the two designs.

**Table 2-3 Comparing CSP-MED and PV-RO [32] [33] [34] [35]**

Characteristic	CSP-MED	PV-RO
Energy input	Heat and Electric	Electric

<b>Energy use</b>	thermal: 60–70 kWh/m <sup>3</sup> electrical: 1.5–2 kWh/m <sup>3</sup>	electrical: BW : 0.5–1.5 kWh/m <sup>3</sup> SW : 4–5 kWh/m <sup>3</sup>
<b>Operation temperature</b>	70°C	Room temperature
<b>Production Cost</b>	2.3-2.9 USD/m <sup>3</sup>	6.5-9.1 USD/m <sup>3</sup> BW 11.7-15.6 USD/m <sup>3</sup> SW
<b>Capacity</b>	>5,000 m <sup>3</sup> /day	<100 m <sup>3</sup> /day
<b>Water quality</b>	≤10 ppm	350-500 ppm
<b>Storage</b>	Thermal storage (≤15 hrs)	Batteries
<b>Development Status</b>	R&D	Application / R&D

### 3. ANALYSIS AND DISCUSSIONS:

If we look at the site specific data in Al Khafji, the following must be considered: Its GHI Annual Average is **5,534 Wh/m<sup>2</sup>** and DNI Annual Average is **4,728 Wh/m<sup>2</sup>** [36] Water demand is close to **30,000 m<sup>3</sup>/day**.

*Energy input:* the location has solar irradiance that is sufficient to produce heat and electricity to couple a desalination plant, as well as access to the electricity grid, so both CSP-MED and PV-RO are possible.

*Energy use:* CSP-MED uses thermal and electrical whereas PV-RO uses only electrical.

*Operation temperature:* CSP-MED operates at a much higher temperature than PV-RO which operates at room temperature.

*Production Cost:* CSP-MED will cost much less than PV-RO according to table 2-2

*Energy input:* the overall energy input including both electrical and thermal for CSP-MED is much more than PV-RO.

*Capacity:* CSP-MED is capable of producing much more than PV-RO. Although more modules could be added, however, the land use requirement for CSP is bigger than PV as indicated before.

*Water quality:* CSP-MED produces better quality water than PV-RO.

*Storage:* CSP-MED is more compatible with thermal storage and PV-RO can be retrofitted with batteries. Challenges tied with energy storage could be solved by using alternative storage such as storing water in tanks, however, this also comes at the cost of upsizing the plant.

*Development status:* CSP-MED is still in R&D phase whereas PV-RO has application.

If we consider the differences between the two systems and realize the inherent advantages of each system, the choice between the two will depend on the priorities in Al Khafji. If we start with the solar resource in Al Khafji, which has a higher GHI than DNI, that suggests PV is better suited than CSP.

However, if we consider other factors the comparison looks different. The size of the capacity needed in Al Khafji is 30,000 m<sup>3</sup>/day, a PV-RO typical capacity is less than 100 m<sup>3</sup>/day whereas CSP-MED has a typical capacity of more than 5000 m<sup>3</sup>/day. Also,

the water demand in Al Khafji is for drinking water which suggest a better quality of water, CSP-MED as we have seen provides a higher purity and better quality water of less than 10 ppm, whereas PV-RO gives a water quality of 350-500 ppm. Of course, this is still potable water that meets the US EPA limit of 500 ppm. Although water quality is decided upon based on the use of water, the produced water could be mixed with ground water, such as the case in Saudi Arabia. Finally, the production cost of CSP-MED is much lower 2.3-2.9 USD/m<sup>3</sup> than that of PV-RO for SW 11.7-15.6 USD/m<sup>3</sup>.

From this simple analysis we could conclude that there are many more advantages enjoyed from the CSP-MED system for Al Khafji location over that of a PV-RO system.

### 4. ACKNOWLEDGMENTS

We wish to thank the Center for Clean Water and Clean Energy at MIT & KFUPM for the Ibn Khaldun fellowship granted to the first author.

### 5. References

- [1] World Bank, "MENA Development Report: Renewable Energy Desalination," World Bank, Washington, D.C., 2012.
- [2] Food and Agriculture Organization of the United Nation, "Groundwater Management in Saudi Arabia: Draft Synthesis Report," FAO, UN, Rome, 2009.
- [3] KACARE, "King Abdullah City for Atomic and Renewable Energy Strategy and Roadmap," in *Value Localizaion Series*, Riyadh, 2013.
- [4] World Bank, "A Water Sector Assessment Report on the Countries of the Cooperation Council of the Arab States of the Gulf," The World Bank, Washington, DC, 2005.
- [5] National Water Company, "Facts and Figures," National Water Company, 2011. [Online]. Available: <http://www.nwc.com.sa/English/Awareness/CSR/WaterConservation/Pages/FactsAndFigures.aspx>. [Accessed 18 07 2014].
- [6] DLR, "Concentrating Solar Power for Seawater Desalination," Federal Ministry for the Environment, Nature Conservation and Nuclear Safety, Germany, 2007.
- [7] Global Water Intelligence, "Becoming a world-class water utility," 2011.
- [8] FICHTNER, "MENA Regional Water Outlook: Desalination Using Renewable Energy," FICHTNER, Stuttgart, Germany, 2011.
- [9] Global Water Intelligence, "Global Water Market 2011: Saudi Arabia," GWI, Oxford, 2011.
- [10] E. Elhadj, "Saudi Arabia's Agricultural Project: From Dust to Dust," 3 June 2008. [Online]. Available: [http://www.gloria-center.org/2008/06/elhadj-2008-06-03/#\\_edn20](http://www.gloria-center.org/2008/06/elhadj-2008-06-03/#_edn20).
- [11] "Saudi Arabia's Great Thirst," National Geographic, [Online]. Available:

<http://environment.nationalgeographic.com/environment/freshwater/saudi-arabia-water-use/>. [Accessed 09 July 2014].

- [1] E. Elhadj, Experiments in Achieving Water and Food Self-Sufficiency in the Middle East: The Consequences of Contrasting Endowments, Ideologies, and Investment Policies in Saudi Arabia and Syria, Florida: Dissertation.com, 2006.
- [1] IDA, "The state of desalination," in *Desalination: sustainable solutions for a thirsty planet*, Perth, 2011.
- [1] O. Buross, *The ABCs of Desalting*, Second ed., Topsfield, Mass.: International Desalination Association, 2000.
- [1] J. E. Miller, "Review of Water Resources and Desalination Technologies," Sandia National Laboratories, Albuquerque, NM, 2003.
- [1] M. A. Darwish and N. M. Al-Najem, "Energy consumption by multi-stage flash and reverse osmosis desalters," *Applied Thermal Engineering*, vol. 20, no. 5, pp. 399-416, 2000.
- [1] H. M. Ettouney, H. T. El-Dessouky and I. Alatiqi, "Understand thermal desalination," *Chemical Engineering Process*, vol. 95, no. 9, pp. 43-54, 1999.
- [1] K. E. Thomas, "Overview of Village Scale, Renewable Energy Powered Desalination.," NREL Report No. TP-440-22083, 1997.
- [1] F. A.-J. H El-Dessouky, "Effectiveness of a thermal energy storage system using phase-change materials," *Energy Conversion and Management*, vol. 38, no. 6, pp. 601-617, 1997.
- [2] A. T. M. P. P. Glueckstern, "The impact of R&D on new technologies, novel design concepts and advanced operating procedures on the cost of water desalination," *Desalination*, vol. 139, no. 1, pp. 217-228, 2001.
- [2] R. Semiat, "Desalination: Present and Future," *Water International*, vol. 25, no. 1, p. 54-65, 2000.
- [2] F. Al-Juwayhel, H. El-Dessouky and H. Ettouney, "Analysis of single-effect evaporator desalination systems combined with vapor compression heat pumps," *Desalination*, vol. 114, no. 3, pp. 253-275, 1997.
- [2] R. V. Wahlgren, "Atmospheric water vapour processor designs for potable water production: a review," *Water Resources*, vol. 35, no. 1, p. 1-22, 2001.
- [2] J. Bednarski, M. Minamide and O. J. Morin, "World Congress on Desalination and Water Science," in *IDA*, Madrid, 1997.
- [2] H. M. E. a. A. C. Lucio Rizzuti, "Solar Desalination for the 21st Century," Springer, Dordrecht, The Netherlands, 2006.
- [2] H. E. F. P. R. A. Muhammad Tauha Ali, "A comprehensive techno-economical review of indirect solar desalination," *Renewable and Sustainable Energy Reviews*, vol. 15, no. 1, pp. 4187-4199, 2011.
- [2] L. Gracia-Rodriguez, A. I. Palmero-Marrero and C. Gomez-Gamacho, "Comparison of solar thermal technologies for applications in seawater desalination," *Desalination*, vol. 142, pp. 135-142, 2002.
- [2] DLR, "Renewable Energy Resources," DLR, Vienna, 2010.
- [2] Solar Consulting Services, "Direct Normal Irradiance for CSP/CPV: Modeling Challenges," International Solar Energy Society, 2013.
- [3] R. Meyer, "Uncertainties of solar resources and their influence on yield of CSP and PV plants," Suntrace, Santiago, Chile, 2001.
- [3] NREL, "Land-Use Requirements for Solar Power Plants in the United States, NREL/TP-6A20-56290," NREL, Golden, CO, 2013.
- [3] IRENA, "Water desalination using renewable energy: Technology brief," IEA-ETSAP and IRENA, 2012.
- [3] FICHTNER, "MENA Regional Water Outlook: Desalination Using Renewable Energy," FICHTNER, Stuttgart, Germany, 2011.
- [3] DLR, "Concentrating Solar Power for Seawater Desalination," Federal Ministry for the Environment, Nature Conservation and Nuclear Safety, Germany, 2007.
- [3] P. e. al, "Roadmap for the development of desalination powered by renewable energy," FRAUNHOFER VERLAG, 2010.
- [3] KACARE, "Renewable Resource Atlas," KACARE, Riyadh, 2015.
- [3] IRENA, "Water desalination using renewable energy: Technology brief," IEA-ETSAP and IRENA, 2012.
- [3] Renewable Resource Atlas of Saudi Arabia, "Renewable Resource Data for Al Khafji," King Abdullah City for Atomic and Renewable Energy, Riyadh, 2014.

# Indirect solar drying: Theoretical study and experimental validation

R Khama<sup>1,2</sup>, F Aissani<sup>1</sup> and R Alkama<sup>3</sup>

<sup>1</sup>Laboratoire de Génie de l'Environnement, Faculté de Technologie, Université de Bejaia, 06000 Bejaia, Algeria

<sup>2</sup>Univ. Ouargla, Fac. Sciences Appliquées, Lab. Génie des Procédés, Ouargla 30000, Algeria

<sup>3</sup>Laboratoire de Génie Électrique, Faculté de Technologie, Université de Bejaia, 06000 Bejaia, Algeria

E-mail: [redkhama@yahoo.fr](mailto:redkhama@yahoo.fr)

**Abstract.** In this paper, we present a numerical simulation of a unidimensional study of food drying by using indirect solar drying technique. The apparatus considered is an indirect solar dryer designed and realized at Laboratory of Process Engineering (University of Ouargla) in the south-east of Algeria. The wet product is deposited in thick layer and is exposed to air convection, its geometry changes during process so shrinkage must be considered. The media is porous and then transfers equations in porous media describe the coupled heat and mass transfers. The study relates to two mathematical models, the first one is for the solar collector and is based on all its energy balances and the other relates to the drying chamber and is based on equations of mass and energy balances. The theoretical analysis gives two systems of differential equations which are difficult to solve using analytical method. These systems of equations are solved implicitly using the finite difference method. A computer program in FORTRAN is developed to simulate the indirect solar drying. The study highlighted well the effect of ambient air parameters on temperatures and efficiency of the solar collector. Air velocity in the porous media is not constant during drying and consequently shrinkage effect is largely happening. The drying kinetics study confirmed the importance of this phenomenon. The simulation models are validated by comparing some simulation results with the experimental results. In addition, the computer program developed in this study can be used with similar solar drying systems.

**Keywords:** Indirect solar drying, Simulation, Experimentation, Solar collector, Drying chamber, Porous media, Heat and mass transfers, Shrinkage, Kinetics.

## 1. Introduction

The production of many fruits and vegetables is seasonal and therefore they are only available for a short time in the year. When production exceeds the absorption capacity of the market to avoid wastage and loss of income for farmers, it is desirable to transform and keep the surplus without neglecting the high prices of a lot of products outside their harvest periods. Dehydration is a very

interesting technique for preserving fruits and vegetables, this is the healthiest conservation and the most significant process for this aim, since it has a great effect on quality of the dried products; indeed vitamins are preserved and can be rebuilt later by dipping.

The principal objective in the drying of the agricultural products is the reduction of the contents of moisture on a level or storage over one prolonged period is possible. It is an operation which consists in removing all the water of the body known as moisture other than its water of hydration [1]. With this intention, generally, we have recourse to appropriate provisions: solar dryers. The majority of the developed solar driers are intended for the agricultural products and their selection is determined by required qualities, characteristics of the product and economic factor.

Solar dryers can be classified as natural convection solar dryers and forced convection solar dryers. In the natural convection solar dryers, the airflow is usually established by buoyancy- induced airflow while in forced convection solar dryers, the airflow is provided by using fan either operated by electricity/solar module or fossil fuel [2].

The process of industrial drying is closely related on the knowledge and the control of the phenomena of coupled transfers of heat and mass occurring between the drying air and the wet product. To dry wet materials is a complicated process always implying these simultaneous and coupled phenomena and to simulate the process by a mathematical modeling would be good and interesting procedure.

In this study, a numerical method is developed where the heat and mass transfer between a porous media (bed of fruit) and an external air flow (drying air), to be predetermined, is treated. The variation of the air velocity is injected into the model and then simulation models are validated by comparing some simulation results with the experimental results.

## Nomenclature

$C_p$ :	Specific heat	[J / Kg .K]
$D$ :	Distance between the cover and the absorber of the collector	[m]
$G$ :	Specific mass flow rate of the air in the collector	[Kg/s.m]
$I_G$ :	Solar radiation	[w/m <sup>2</sup> ]
$L$ :	Length	[m]
$\ell$ :	Width	[m]
$M$ :	Moisture content of the product	[Kg H <sub>2</sub> O/Kg dm]
$T_{amb}$ :	Temperature of ambient air	[K]
$T_a$ :	Temperature of the air in the collector	[K]
$T_b$ :	Temperature of the absorber	[K]
$T_c$ :	Temperature of the cover	[K]
$T_p$ :	Temperature of the product	[K]
$t$ :	Time	[s]
$U_b$ :	Heat loss coefficient through the back side of the collector to ambient air	[W/m <sup>2</sup> .K]
$W$ :	Absolute humidity of the air	[Kg/Kg da]
$\alpha_{,bf}$ :	Convective heat transfer coefficient between the absorber and the air	[W/m <sup>2</sup> .K]
$\alpha_{,cf}$ :	Convective heat transfer coefficient between the cover and the air	[W/m <sup>2</sup> .K]
$\alpha_{,bc}$ :	Radiative heat transfer coefficient between the cover and the absorber	[W/m <sup>2</sup> .K]
$\alpha_{,cs}$ :	Radiative heat transfer coefficient between the cover and the sky	[W/m <sup>2</sup> .K]
$\alpha_{,ca}$ :	Convective heat loss coefficient of the cover caused by wind	[W/m <sup>2</sup> .K]
$\beta$ :	Absorption coefficient of the cover	[/]
$\delta$ :	Thickness	[m]
$\varepsilon$ :	Emittance	[/]
$\rho$ :	Density	[kg/m <sup>3</sup> ]
$(\tau\theta)$ :	Transmittance-absorptance product of the system consisting of the cover and the absorber	[/]

## 2. Material

Figure 1 is a photo and a schematic diagram of the simulated indirect solar dryer, mainly made up of two parts: flat-plate solar collector and drying chamber; it is also, the apparatus used in experimental validation. The hot air goes up by natural or forced convection until drying chamber and duration of drying is very variable according to climatic conditions.

The solar collector, making it possible to heat air in the part ranging between transparent glass cover and absorber plate, has as total dimensions 190 X 114 X 16 cm. The back part and the side walls are insulated with glass wool. The absorber is a copper plate painted in matt black color which must transmit energy collected to the air by avoiding all losses (by conduction - convection - radiation) of the various peripheral parts towards outside.

The drying chamber is a parallelepiped cupboard of total size 114 X 114 X 166 cm and from which walls out of coated sheet and are also insulated with glass wool. It is posed on a metal support rolling to a height of 1 m of the ground, making it possible to obtain the orientation desired during drying. It comprises four sites of trays being used to carry the wet product to dry. The drying chamber ends by a chimney being used to evacuate the humid air naturally or in mode forced with a fan.

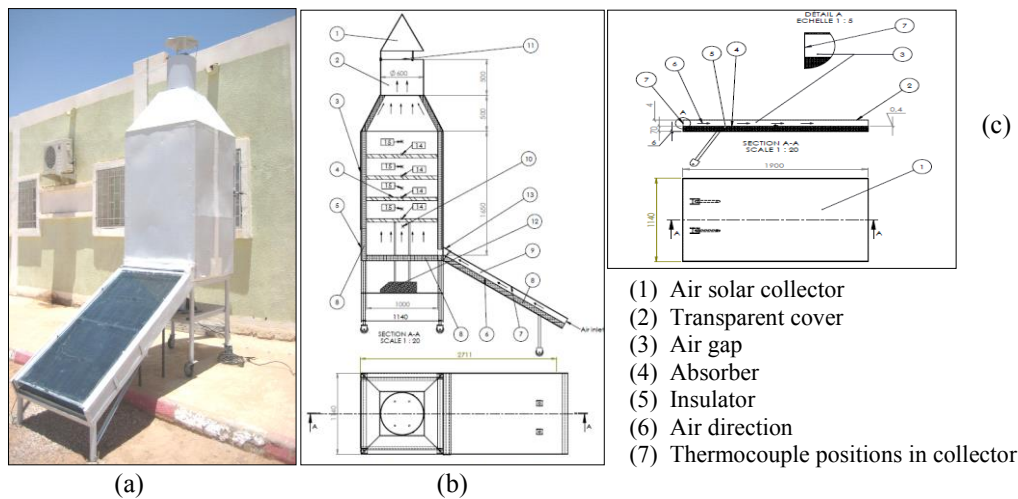


**Figure 1:** Schematic diagram and photo of the indirect solar dryer [3]  
 (a) Photo (b) Schematic diagram (c) Diagram of the solar collector

## 3. Mathematical modeling

### 3.1. First model [4,5,6]

Figure 2 is a schematic diagram showing heat transfers in the solar collector.

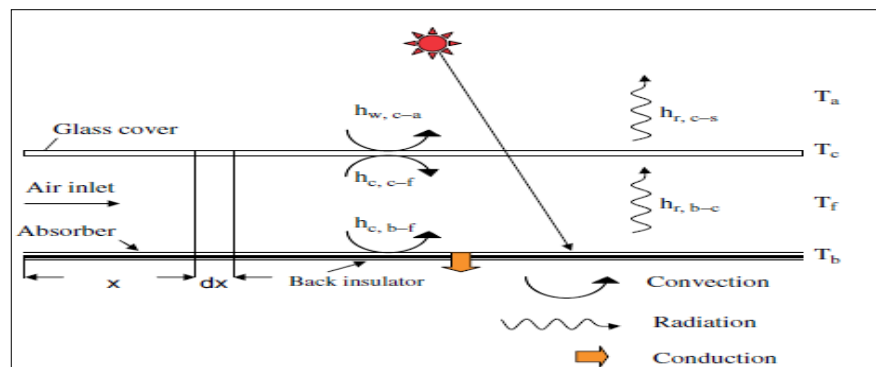


**Figure 2:** Heat transfers in the solar collector [4]

### 3.1.1. Equations of the solar collector

- At the cover:

$$\rho_c \cdot \delta_c \cdot CP_c \frac{\partial T_c}{\partial t} = \alpha_{r,bc} (T_b - T_c) + \alpha_{c,ac} (T_a - T_c) + \alpha_{w,ca} (T_{amb} - T_c) + \alpha_{c,ac} (T_s - T_c) + \beta \cdot I_G \quad (1)$$

- At the air gap:

$$D \cdot G \cdot CP_a \frac{\partial T_a}{\partial x} = \alpha_{c,ca} (T_c - T_a) + \alpha_{c,ba} (T_b - T_a) \quad (2)$$

- At the absorber

$$\rho_b \cdot \delta_b \cdot CP_b \frac{\partial T_b}{\partial t} = \alpha_{c,ba} (T_a - T_b) + \alpha_{r,bc} (T_c - T_b) + U_b (T_{amb} - T_b) + (\tau \beta) \cdot I_G \quad (3)$$

### 3.1.2. Calculation of the heat transfer coefficients

- Radiative heat transfer coefficient between the cover and the sky  $\alpha_{r,cs}$  is calculated using the following equation:

$$\alpha_{r,cs} = \varepsilon_c \sigma (T_c^2 - T_s^2) (T_c + T_s) \quad (4)$$

$$\text{where: } T_s = 0.552 T_a^{1.5} \quad (5)$$

- Radiative heat transfer coefficient between the cover and the absorber  $\alpha_{r,bc}$  is calculated using the following equation:

$$\alpha_{r,bc} = \frac{\sigma (T_b^2 + T_c^2) (T_b + T_c)}{\frac{1}{\varepsilon_b} + \frac{1}{\varepsilon_c} - 1} \quad (6)$$

- Convective heat loss coefficient of the cover  $\alpha_{w,ca}$  caused by wind is given by :

$$\alpha_{w,ca} = 5.7 + 3.8 v \quad (7)$$

- The coefficient of heat transfer  $\alpha_{c,ba}$  is calculated from:

$$\alpha_{c,ba} = \frac{N_u \cdot \lambda_a}{dh} \quad (8)$$

The collector is a system of differential equations which are difficult to solve using analytical methods. This system of equations was solved implicitly using the finite difference method.

## 3.2. Second model [1,7-11]

### 3.2.1. Equations of the drying chamber

- Mass balance (wet air) :

$$\rho_a \left[ \xi \frac{\partial W}{\partial t} + v \frac{\partial W}{\partial x} + (1 - \xi) \rho_p \frac{\partial M}{\partial t} \right] = 0 \quad (9)$$

- Enthalpic balance (wet air) :

$$\rho_a \left[ CP_a + W \cdot CP_v \right] \left[ \xi \frac{\partial T_a}{\partial t} + v \frac{\partial T_a}{\partial x} \right] = A I \alpha_c (T_p - T_a) - (1 - \xi) \rho_p CP_v (T_p - T_a) \frac{\partial M}{\partial t} \quad (10)$$

- Enthalpic balance (wet fruit) :

$$(1 - \xi) \rho_p (C_{p_p} + M C_{p_e}) \frac{\partial T_p}{\partial t} = A_l \alpha_c (T_a - T_p) + H \rho_p (1 - \xi) \frac{\partial M}{\partial t} \quad (11)$$

The result is a system with four unknown variables ( $T_a, T_p, W$  and  $M$ ) and two variables ( $x$  and  $t$ ), the equations are supplemented by that of drying kinetics equation:

$$\frac{\partial M}{\partial t} = K (M - M_{eq}) \quad (12)$$

The drying chamber is, then, a system of differential equations which are difficult to solve using analytical method. This system of equations was solved implicitly using the finite difference method (as the collector model).

### 3.2.2. Calculation of the drying constants

- The model of Henderson and Pabis is selected for the kinetics:

$$MR = \frac{M(t) - M_{eq}}{M_0 - M_{eq}} = A \cdot \exp(Kt) \quad (13)$$

- The values of the coefficient  $K$  are approximated by the simple equation Arrhenius:

$$K = K_0 \exp \left( \frac{E_a}{R_g (T_a + 273)} \right) \quad (14)$$

- $K_0$  is a given coefficient, according to the drying air velocity by:

$$K_0 = 1341.2 \exp(2.8404 v) \quad (15)$$

- $E_a$  is the energy of activation given according to  $v$  by:

$$E_a = \frac{(34.037663 \times 14407.625) + (48.47102 \times v^{15.96189})}{14407.625 + v^{15.96189}} \quad (16)$$

- Finally, constant  $A$  is given, according to  $v$  and  $T_a$ , by:

$$A = \left( 0.000104 T_a^2 - 0.012291 T_a + 0.256909 \right) v^2 + \left( 0.000203 T_a^2 + 0.021976 T_a - 0.302885 \right) v + \left( 0.000059 T_a^2 - 0.002967 T_a + 0.765417 \right) \quad (17)$$

### 3.2.3. Calculation of the drying air velocity [1,13]

The air velocity  $v$  is calculated as follows:

$$v = \frac{v_o}{\xi} \quad (18)$$

The porosity  $\xi$  is calculated using the following equation:

$$\xi = 1 - OC \quad (19)$$

$OC$  is the occupancy rate and is defined as the relationship between the volume occupied by the spheres on a tray and the volume of the parallelepiped with dimension  $L \times \ell \times d_p$ :

$$OC = \frac{N_p \pi d_p^3}{6 L \ell d_p} \quad (20)$$

$d_p$  is the diameter of the product calculated by :

$$d_p = \frac{6 V_p}{N_p \pi}^{1/3} \quad (21)$$

$N_p$  is the constant number of spheres in the layer  $j$  such as:

$$N_p = \frac{L}{d_{p0}} \times \frac{\ell}{d_{p0}} \quad (22)$$

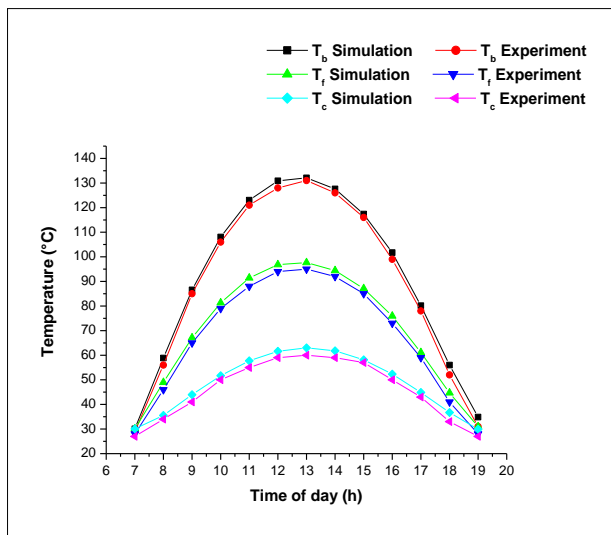
$V_p$  is the volume of the fruit on the tray  $j$  calculated as follows:

$$V_p = \frac{m_{ph}}{\rho_p} \quad (23)$$

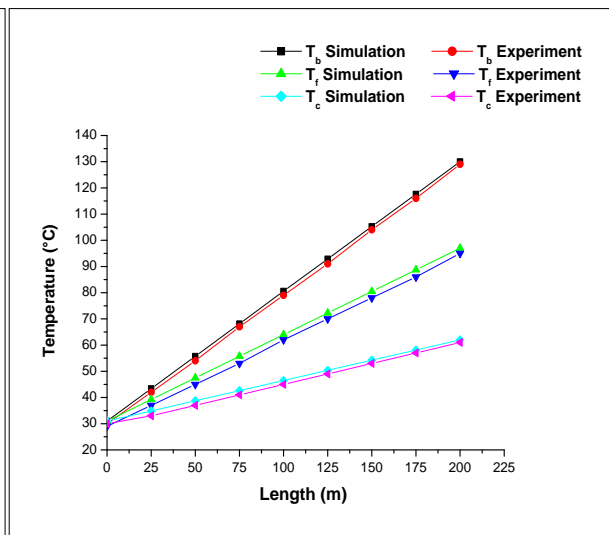
#### 4. Results and discussions

Figure 3 shows the temporal evolutions of the temperature in the various components of the collector and in its various points during the day. These evolutions are directly proportional to the solar radiation while being very sensitive to its variations, as well as the absorber temperature is always higher than the air and cover temperatures in all the points, the three reach their maximum values between noon and 2:00 pm. The difference in temperature is preserved at the moment that the incidental radiation exists. The temperature in the various layers of the collector increases according to the length (See Figure 4).

As observed from figures 3 and 4, there is an excellent agreement between the experimental and numerical results.



**Figure 3:** Variation of the solar collector temperatures v.s. time



**Figure 4:** Variation of the solar collector temperatures v.s. length

Figure 5 is a comparison between two calculations which were made: with and without shrinkage. The importance of the introduction of this phenomenon is very clear and its negligence leads to incorrect results, for example:

At  $t = 10$  h ;

$M = 1.79514 \text{ Kg / Kg } dm$  (With shrinkage) whereas one is hardly with

$M = 2.736 \text{ Kg / Kg } dm$  (Without shrinkage).

At  $t = 20$  h ;

$M = 1.10947 \text{ Kg / Kg } dm$  (With shrinkage) whereas one is hardly with

$M = 1.982 \text{ Kg / Kg } dm$  (Without shrinkage).

$M_{eq}$  is reached in 75.5 h (with Shrinkage) but when the shrinkage is neglected  $M_{eq}$  is reached only after 110 h, then 35.5 h of difference

The cause of this error resides at the level of the calculation drying air velocity  $v$  through the layer of the wet product, which is considered constant in the first case (without shrinkage) whereas it is not it in truth : it is a function of the porosity which is itself function of the diameter variable during drying.

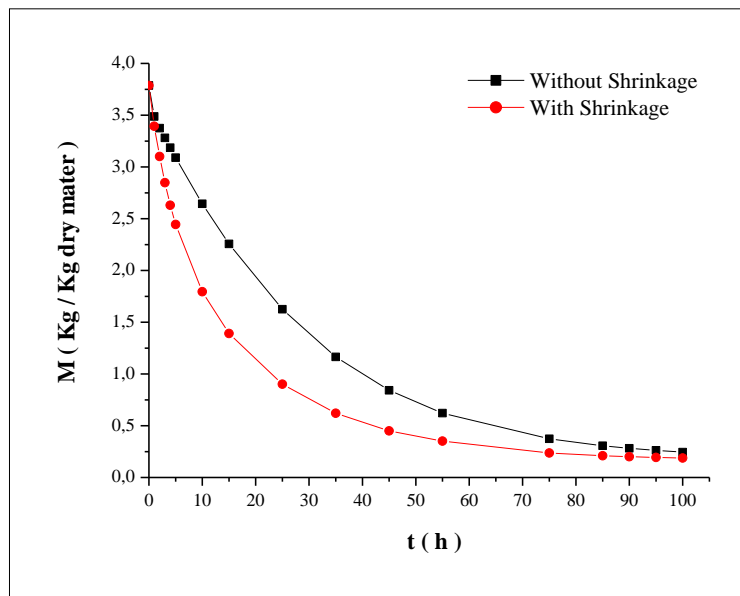


**Figure 5:** Effect of shrinkage on Solar drying kinetics

## 5. Conclusions

The study highlighted well the effect of ambient air parameters on temperatures and efficiency of the solar collector. Air velocity in the porous media is not constant during drying and consequently shrinkage effect is largely happening during process.

The drying kinetics study confirmed the importance of this phenomenon.

The simulation models are validated by comparing some important simulation results with the experimental results.

In addition, the computer program developed in this study can be used with similar solar drying systems.

## References

- [1] Daguinet M. (1985), Solar dryers: theory and practical (in French), UNESCO
- [2] Janjai S. and Bala B. K., (2012), Solar Drying Technology, Food Engineering Reviews, 4, pp. 16-54.
- [3] Khama R., Aissani F. and Alkama R., (2013), Experimental study and performance testing of an indirect solar dryer, The International Chemical Engineering Congress Djerba, Tunisia.
- [4] Smitabhindu R., Janjai S., and Chankong V., (2008), Optimization of a solar – assisted drying system for drying bananas, Renewable Energy 33, pp. 1523-1531.
- [5] Duffie J.A., and Beckman W.A. (1991), Solar engineering of thermal process " New York: Wiley.
- [6] Mc Adams W.H., (1954), Heat transmission 3 rd edition New York : Mc Graw – Hill.
- [7] Arnaud G., and Fohr J.-P., (1988), Slow drying simulation in thick layers of granular products, Int. J. Heat Mass Transfer. Vol. 31, No. 12, pp. 2517-2526.
- [8] Ratti C., and Mujumdar A.S., (1995), Simulation of packed bed drying of foodstuffs with airflow reversal, Journal of Food Engineering 26, pp. 259-271.
- [9] Babalis S.J., and Belessiotis V.G., (2004), Influence of the drying conditions on the drying constants and moisture diffusivity during the thin-layer drying of figs, Journal of Food Engineering, 65, pp. 449-458.
- [10] Azzouz S., (2002), Moisture diffusivity and drying kinetic equation of convective drying of grapes", Journal of Food Engineering, 55, pp. 323-330.
- [11] El- Sebail A.A., (2002), Empirical correlation for drying kinetics of some fruits and vegetables, Energy, 27, pp. 845-859.
- [12] Bennamoun L., and Belhamri A., (2006), Numerical simulation of drying under variables external conditions: Application to solar drying of seedless grapes", Journal of Food Engineering, 76, pp. 179-187.

# Theoretical study of a solar-assisted ejector cooling system with refrigerant ammonia

Z.Saadi<sup>1</sup>, H.Soualmi<sup>1</sup>, A. Rahmani<sup>1</sup>

<sup>1</sup>Unit of Research in Renewable Energies in the Saharan Medium, CDER-EPST, URER-MS, Adrar 01000, Algérie, B.P 478, Road of Reggane - Adrar. Algeria.

E-mail :saadi\_zine@yahoo.fr

**Abstract:** A solar ejector cooling system is one of the most promising technologies because of its simplicity, its low initial costs and the use of a free heat source (solar energy). In this work, a theoretical study was carried out to evaluate the performances of an ejector refrigeration cycle driven by solar energy functioning with average temperature where the working fluid is ammonia (R717). Ejector dimensions were also calculated using the constant pressure mixing ejector theory.

For a given cooling capacity of 10 KW, temperatures: generator, condenser, evaporator and superheat fixed, Nozzle and diffuser efficiencies were taken as 0.95, 0.75 respectively, entrainment ratio, main geometrical parameters of ejector and the ejector cooling machine performance are calculated using meteorological databases of the site Adrar in south of Algeria such as the solar irradiation and the ambient temperature.

The effect of generator, condenser and evaporator temperatures on COP are analyzed. The results showed that the COP an optimum COP can be achieved with the generator temperature using three different collectors A, B et C.

Keywords:Ejector; Cooling system; Solar energy; COP; ammonia.

## I. INTRODUCTION

Approximately 15% of the world electricity consumption is used for refrigeration and air-conditioning applications (L. Lucas,1988). The demand for air-conditioning is proportional to the solar radiation, thus utilization of solar energy is a logical way to meet the increasing demand for cooling.

Several existing technologies can be applied for the conversion of the solar radiation for the refrigeration or air-conditioning. Among the processes of thermal transformation of solar energy, ejector refrigeration is one of the most promising technologies because of

its relative simplicity and low capital cost when compared to other system.

Several studies were carried out on the solar-driven ejector refrigeration systems. Abdulateef et al. (2009) conducted a review on solar assisted ejector cooling technologies. The influence of ejector geometry, refrigerant nature and operating conditions on system performance was assessed. It was shown that a dynamic simulation of the system operation is required for correct design of the equipment, rather than a steady state analysis.

Vidal et al. (2006) and more recently Vidal and Cole (2010) performed a TRNSYS hourly simulation of a solar assisted ejector cooling system with hot storage. It was found that important savings in auxiliary energy can be achieved by increasing the solar collector area. The capacity of the storage tank was also a factor affecting the amount of auxiliary energy required.

The major components of the solar collector circuit are the collector array, a hot water storage tank and the ejector cycle as it is showing in the figure1.

In practice, the solar collector is used to absorb thermal energy initially. Recovered heat is then used in a refrigeration machine to produce the cold.

A theoretical work on collector selection can be found in Huang et al.(2001), for different operating conditions, using R141b as the working fluid. It was concluded that the high price of vacuum tube collectors makes the use of flat-plate collectors economically more attractive, in spite of their lower efficiency.

Huang et al. (1998) developed a solar ejector cooling system using R141b as the re-

frigerant; obtaining the overall  $COP$  of around 0.22 at a generating temperature of  $95^{\circ}\text{C}$ , an evaporating temperature of  $8^{\circ}\text{C}$  and solar radiation of  $700\text{W}\cdot\text{m}^{-2}$ .

Alexis et al (2005) focused their research to investigate the performance of an ejector cooling system driven by solar energy and having R134a as working fluid. It was found that the  $COP$  of overall system varied from 0.014 to 0.101 with the same operation conditions and total solar radiation ( $536\text{--}838\text{ W/m}^2$ ) in July.

S.Varga et al. (2009) presented a theoretical study to evaluate the performance of a solar-driven ejector cycle using water as operating fluid. The results indicated that in order to achieve an acceptable coefficient of performance, generator temperatures should not fall below  $90^{\circ}\text{C}$ .

This paper presents a theoretical analysis of the performance a solar-driven ejector cycle. The model used a simplified 1D approach based on energy, mass and momentum conservation equations and a constant-pressure mixing is assumed to occur inside the constant-area section of the ejector. The current model is based on the NIST-REFPROP database for refrigerants properties calculations using the meteorological databases of the site Adrar Algeria such as the solar irradiation and the average ambient temperature.

## I. DESCRIPTION OF THE SOLAR EJECTOR OF REFRIGERATION CYCLE

The ejector is a thermally driven compressor that operates in a heat pump refrigeration cycle. In a heat pump system, the ejector takes the place of the electrically driven compressor, but uses heat rather than electricity to produce the compression effect.

The solar ejector refrigeration cycle is shown in Fig. 1 and in diagram P,h in figure 2. It comprises of two loops, one is solar collection loop which is the main energy source of ejector refrigeration system (ERS) and the other is ejector refrigeration loop

which supplies useful cooling to the user. The solar collection loop is composed of collector, a hot water storage tank and a circulating pump.

The ejector refrigeration loop consists of two subsystems: the power subsystem, and the refrigeration subsystem. In the power subsystem, the refrigerant flows through the generator, the ejector, the condenser and the circulating pump, and finally flows back to the generator to supply high pressure motive fluid to the ejector. In the refrigeration subsystem, the refrigerant flows through the ejector, the condenser, the expansion valve, the evaporator, and then back to the suction of the ejector to supply the required cooling capacity. The main part of the ejector refrigeration loop is the ejector (Fig. 2), which is composed of a convergent–divergent nozzle, suction chamber, mixing chamber and a diffuser. The motive fluid is first accelerated to supersonic velocity in the convergent–divergent nozzle, which entrains the evaporated fluid (named entrained fluid) from the evaporator and the two fluids mix together in the mixing chamber. In the diffuser, the velocity of the mixed fluid is stepped down and the pressure is lifted to the condenser pressure.

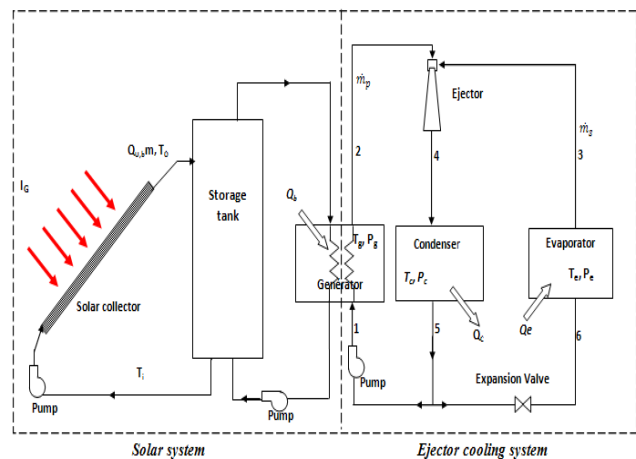


Fig. 1: Ejector cooling system assisted by solar energy.

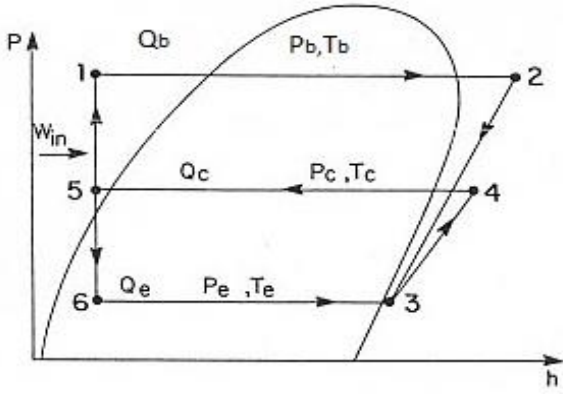


Fig. 2: Ejector cooling system assisted by solar energy in diagram P, h.

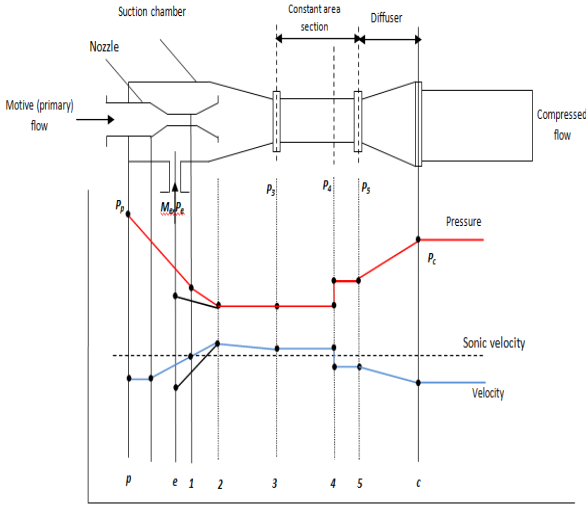


Fig. 3: Variation in stream pressure and velocity as a function of location along the ejector.

## II. SOLAR COLLECTOR SUBSYSTEM

Useful heat  $Qu$ , recovered by the solar collector, is calculated Hottel-Whillier-Bliss Duffie and Beckman equation, 1991 as follows:

$$Q_u = \eta_{coll} A_{coll} I_G \quad (1)$$

The performance of the solar collector array can be assessed by the solar collector efficiency ( $\eta_{coll}$ ) given by

$$\eta_{coll} = F_R(\tau\alpha) - F_R U_L \left( \frac{T_{e,cap} - T_{amb}}{I} \right) \quad (2)$$

Where  $F_R$  is the collector heat removal factor. The value of factors  $F_R(\tau\alpha)$  and  $F_R U_L$  depend on the type of the collectors, layer of the cover glass and selective material (Pridasawas W2006).

$T_{in,coll}$  and  $T_{amb}$  are the inlet temperatures of solar collector and the ambient temperature where  $T_{in,coll} = T_b + 10$ .

## III. EJECTOR REFRIGERATION CYCLE SUBSYSTEM

The performance of an ejector can be defined in terms of the entrainment ratio or mass flow ratio, which is the ratio between the secondary and the primary fluid mass flow rates:

$$U = \frac{\dot{m}_s}{\dot{m}_p} \quad (3)$$

For a given cooling power of 10 kw, the mass flow rate of secondary flow  $\dot{m}_s$  is given by following equation:

$$\dot{m}_s = \frac{\dot{Q}_e}{(h_3 - h_6)} \quad (4)$$

Throat section area at the secondary flow calculated:

$$\dot{m}_s = \rho_s^* * V_s^* * A_s^* \quad (5)$$

Throat section area of the primary nozzle and section area in plane 1:

$$\dot{m}_p = \rho_p^* * V_p^* * A_p^* \quad (6)$$

$$\dot{m}_s = \rho_{p1} * V_{p1} * A_{p1} \quad (7)$$

The condenser output, pumping and generator power were calculated through:

$$\dot{Q}_c = (\dot{m}_p + \dot{m}_s)(h_4 - h_5) \quad (8)$$

$$\dot{Q}_b = \dot{m}_p(h_2 - h_1) \quad (9)$$

$$W_p = \dot{m}_p(h_1 - h_5) \quad (10)$$

The coefficient of performance of an ejector refrigeration cycle is defined as:

$$COP = \frac{Q_e}{Q_b + W_p} = U \frac{(h_3 - h_6)}{(h_2 - h_5)} \quad (11)$$

The coefficient of performance of a solar ejector cooling cycle of refrigeration  $COP_{sys}$  ejector is expressed by the following equation:

$$COP_{sys} = \eta_{cap} * COP \quad (12)$$

The flow inside the ejector is steady and one dimension; the mixing in the suction cham-

ber occurs in the constant pressure between plans 4 and 5.

In sonic mode (optimal) this pressure is equal to that of the secondary fluid throat (Mach number equal 1) before its mixing with the primary education fluid.

The primary nozzle, entrainment and diffuser efficiencies were taken as 0.95, 0.85 and 0.75, respectively.

In the ejector refrigerating system, the refrigerant at high-pressure vapor state (motive flow) is expanded through the primary nozzle (Fig. 2).

In the primary nozzle, the motive fluid undergoes an adiabatic expansion resulting in a high velocity and low pressure at the exit.

The Velocity  $V$  of the primary fluid at the exit of convergent-divergent nozzle (plane 1) is given by:

$$V_{p1} = \sqrt{2\eta_p(h_{0p} - h_{p1})_{is}} \quad (13)$$

$$h_{p1} = h_{0p} - \eta_p(h_{0p} - h_{p1, is}) \quad (14)$$

Using the constant pressure mixing ejector model by applying momentum and energy balances between planes 1 and 2, the velocity  $V_2$  and Enthalpy  $h_2$  calculated by following equations:

$$V_2 * \dot{m}_2 = V_{p1} * \dot{m}_p + V_s^* * \dot{m}_s \quad (15)$$

$$h_2 * V_2 + \frac{1}{2} * \dot{m}_2 V_2^2 = h_{p1} \dot{m}_p + 1/2 + \dot{m}_p *$$

$$V_{p1}^2 + h_s^* * \dot{m}_s + 1/2 + \dot{m}_p * V_s^{*2} \quad (16)$$

The supersonic mixture at plane 2, a normal shock wave can occur at the end of the mixing chamber between the planes 2 and 3. The Velocity  $V_3$  and Enthalpy  $h_3$  calculated by following equations:

$$V_3 * \dot{m}_2 + P_3 * A_3 = V_2 * \dot{m}_2 + P_2 * A_2 \quad (17)$$

$$h_3 + \frac{1}{2} * V_3^2 = h_2 + 1/2 * V_2^2 \quad (18)$$

The temperature and the pressure of the compressed fluid at the exit of the diffuser (plane 4) can be derived from:

$$h_4 = \frac{h_{0p} + U * h_s}{1 + U} \quad (19)$$

$$\eta_p = \frac{h_{4, is} - h_3}{h_4 - h_3} \quad (20)$$

#### IV. CALCULATION PROCEDURES

The secondary fluid is assumed to reach sonic velocity at the mixing chamber inlet (plane 1). The pressure in plane 1 (P1) is assumed to be uniform and equal to that corresponding to the sonic throat of the secondary jet to this place (Constant pressure flow model).

The superheat at the evaporator exit  $\Delta T_E = 4$  K, and at the generator exit  $\Delta T_G = 3$  K. These superheat values allow to realize dry expansions in the primary and the secondary nozzles.

For temperatures generator  $T_G$ , the condenser  $T_C$  and the evaporator  $T_C$  fixed, the entrained flow rate is given for a refrigerating power of 10 Kw (Eq. (4)) the throat section area  $A_{S1}$  can be deduced then from the equation (5).

For assumed value of the primary flow rate,  $A_p^*$  and  $A_{p1}$  can be calculated using the equations (6) and (7) and consequently  $A_1$  ( $A_1 = A_{p1} + A_{s1}$ ). The resolution of the equations of mixture between the planes (1) and (2) calculate the velocity  $V_2$ , the temperature  $T_2$  and the pressure  $P_2$ . Finally, the equations (19) and (20) leads to a value of the pressure  $P_4$  of the mixture the diffuser exit, which will be adjusted using until equality with condenser pressure  $P_C$ .

#### V. RESULTATS AND DISCUSSION

The monthly average radiation on a horizontal surface and the monthly average ambient temperature by using data from typical meteorological year databases of the Adrar Algeria site are presented in figure 4. It is noticed that whole-body radiation and the ambient temperature are high in the Algerian south (Adrar) [11].

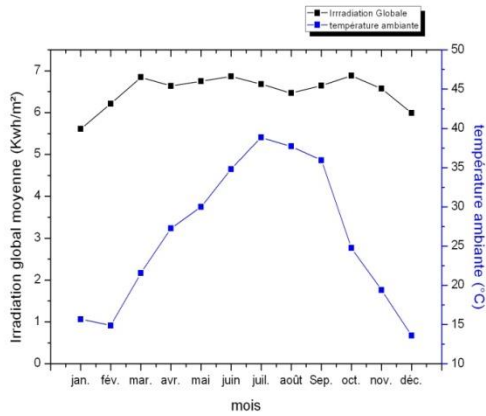


Figure 4. Monthly average daily radiation and monthly average ambient

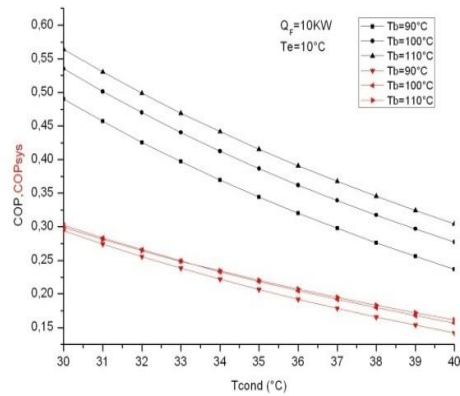


Fig.7: The effect of condenser temperature  $T_c$  under different generator temperatures  $T_g$  on  $COP$  and  $COP_{sys}$ .

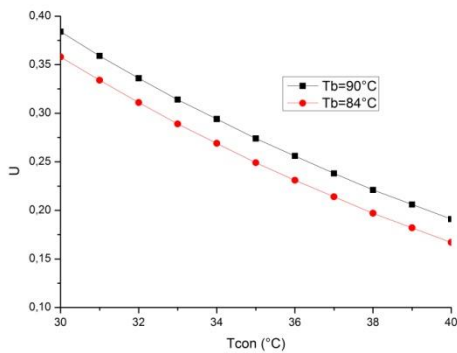


Fig.5: The effect of condensing temperature  $T_c$  under on entrainment factor

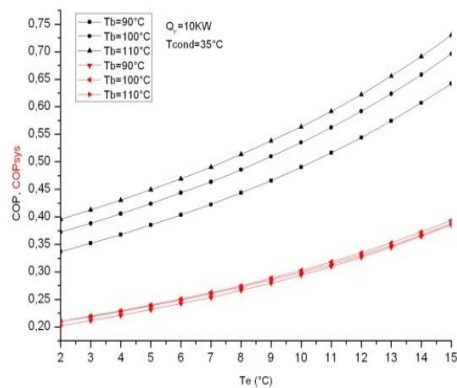


Fig.6: The effect of evaporator temperature  $T_e$  under different generator temperatures  $T_g$  on  $COP$  and  $COP_{sys}$ .

The performance of an ejector can be defined in terms of the entrainment ratio or mass flow ratio, Figure 5 presents the variation of the entrainment ratio according to condenser temperature.

During one day, the solar radiation received by a collector varies typically presented in figure 4. It increases as of the rising of the sun to reach a maximum at solar midday before decreasing again until the night.

In clear times, it is possible to obtain a density flux higher than  $1000 \text{ W/m}^2$  at midday. The solar energy utilization thus is well adapted to the applications for which the requirements in cold coincide with the hours of sunning. The highest radiation is obtained July and low January.

$COP$  and  $COP_{sys}$  as a function of evaporator and generator temperatures are shown in Figure 6 under the operating conditions following; The ejector working at an optimal sonic mode (Boumaraf *et al*, 2007), which replaces a compressor of refrigeration machine, for a compression ratio  $R_c = P_c/P_e = 1,5$ , and evaporator temperature and an superheating fixed at 5 and condenser exit temperature of  $35^\circ\text{C}$  and given cooling power being fixed at 10 kw, the  $COP$  and  $COP_{sys}$  increase with evaporator temperature  $T_e$ , as shown in Figure 3.

For a generator temperature of  $110^\circ\text{C}$ , the evaporator temperature should be about  $7^\circ\text{C}$  or higher to achieve a  $COP$  of at least 0,50. For a generator temperature of  $90^\circ\text{C}$  the evaporator temperature should be as high as  $11^\circ\text{C}$  to obtain the same  $COP$ .

Figure 7 presents the variation of the  $COP$  and  $COP_{sys}$  according to condenser and generator temperatures. It is clear from the

figure that the ejector cooling cycle performance decreases quickly with increasing condenser temperature. Considering the climatic conditions in Adrar Algeria, it is likely that condenser temperatures would be 48°C or higher.

For condenser temperature of 35°C and generator temperature of 90°C the performance coefficient  $COP$  is 0,36, and for generator temperature about 110°C  $COP$  de 0,43.

Figure 8 presents the variation thermal efficiency solar collector efficiency for three different collectors A, B and C, for a solar radiation of 800 W/m<sup>2</sup> it can be seen that the solar collector efficiency C (vacuum tube solar collector) gives better solar collector efficiency than the two other collectors.

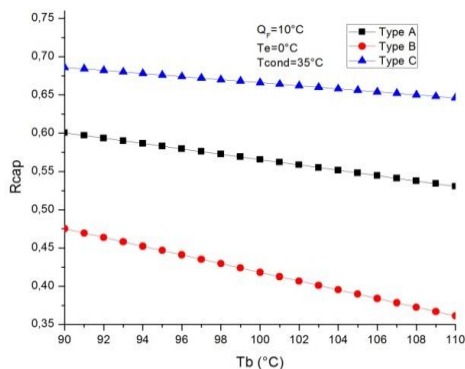


Fig.8: Variation thermal efficiency of solar collector of solar collector A, B, C with generator

## V. CONCLUSION

In this work, a thermodynamic analysis of a solar ejector cooling system was presented by using a one dimensional model 1D for the ejector. The model presented calculate the entrainment ratio of ejector, ejector cooling cycle performance  $COP$  solar ejector cooling system  $COP_{sys}$  for different operating condition. The results indicated that both  $COP$  and system efficiencies increased with generator temperature, within the range considered in this work. In order to obtain acceptable values, generator temperature should not be below 90°C. This would require a collector output temperature of about 100°C. Evacuated tube collectors are better suited for operating an ejector cooling sys-

tem. Evaporator temperature of the evaporator lower than 10°C results a low coefficient from performance.

## REFERENCES

- L. Lucas, IIR news, Int J Refrigeration 21 (2) (1988) 88.) *Review on solar-driven ejector refrigeration technologies Renewable and Sustainable Energy Reviews 13* (2009) 1338–1349
- Review on solar-driven ejector refrigeration technologies Renewable and Sustainable *Energy Reviews 13* (2009) 1338–1349.
- Vidal H, Colle S, Perreira GS. Modelling and hourly simulation of a solar ejector cooling system. *Appl Therm Eng* 2006;26:663–72.
- Vidal H, Colle S. Simulation and economic optimization of a solar assisted combined ejector-vapor compression cycle for cooling applications. *Applied Thermal Engineering* 2010; 30: 478-86.
- Huang BJ, Petrenko VA, Samofatov IYA, et al. Collector selection for solar ejector cooling system. *Sol Energy* 2001;71:269–74.
- Huang BS, Chang JM, Petrenko VA, Zhunk KB. A solar ejector cooling system using refrigerant R141b. *Sol Energy* 1998;64(4–6):223–6.
- G.K. Alexis, E.K. Karayiannis. A solar ejector cooling system using refrigerant R134a in the Athens area. *Renewable Energy* 30 (2005) 1457–1469.
- Szabolcs Varga, Armando C. Oliveira and Bogdan Diaconu. Analysis of a solar-assisted ejector cooling system for air conditioning International *Journal of Low-Carbon Technologies* 2009, 4, 2–8)
- Boumaraf L., Lallemand A., Comparaison des performances optimales d'un éjecteur dimensionné selon les modèle à pressions constante et à section constante. *Actes des 13ème journées internationales de thermique, Albi 2007 Vol 1 pp. 371-375.*)
- NIST Standard Reference Database 23. NIST Thermodynamics and transport Properties of Refrigerants and Refrigerant Mixtures, REFPROP, Version 7.0.
- Pridasawas W. Solar driven refrigeration systems with focus on the ejector cycle. Ph.D. *Thesis. Royal Institute of Technology, Stockholm, Sweden, 2006.*
- Meteorological data for the region of Adrar Algeria.

# Numerical study of heat transfer in solar receivers for CSP

S. Lecheheb,<sup>1,2,\*</sup> A. Bouhallassa,<sup>1</sup> M. Mammari,<sup>1</sup> S. Bouaichaoui<sup>1</sup> and A. Hamidat<sup>1</sup>

<sup>1</sup>Centre de Développement des Energies Renouvelables CDER, BP 62 Route de l'observatoire Bouzaréah 16340, Algiers, Algeria

<sup>2</sup>University of Sciences and Technology Houari Boumediene, Laboratory of Thermodynamics and Energetics Systems, Babezzouar-Algiers, Algeria

e-mail: [s.lecheheb@cder.dz](mailto:s.lecheheb@cder.dz), [lecheheb.sabrina@gmail.com](mailto:lecheheb.sabrina@gmail.com)

**Abstract:** The aims of this study are to assess the position, design, properties and performance of solar receivers (material, coolant ...) in the CSP numerically.

Optimize the operating conditions for increasing the thermal efficiency, improving energy and environmental efficiency of different solar thermal as well as the development of solar concentrator and its components, especially in the "solar tower".

The establishment of a future innovation plan taking into account the results obtained previously and subsequently.

This investigation is explained by a constant research for efficiency in order to find a compromise between a good heat exchange coefficient from the receiver to the heat transfer fluid, the decreasing of radiative and convective heat losses and charges losses negligible or limited.

For that reason, it is necessary to make a receiver modeling (surface, volumetric, external, etc...) and a simulation of heat transfer at their level in order to identify the advantages and disadvantages of the considered receiver that should be the most efficient. We modeled the process to establish the properties related to heat transfer involved the volumetric receiver in the solar tower. Thus using a computational code based on finite volume method (Fluent CFD).

**Keywords:** solar tower, solar receiver, heat transfer fluid HTF, convective heat losses, radiative losses, efficiency, Fluent CFD.

## INTRODUCTION

In a solar tower power plant, the sun radiation is reflected by many heliostats toward a cen-

tral receiver mounted on a tower. The receiver is the most important part of the plant; it absorbs the concentrated solar radiation and transfers it into a heat transfer fluid.

The SOLAR TWO demonstration power plant in Barstow, CA, USA featured the first design, a 42 MWth open receiver that was operated for 14 months in the late 1990. A modern open receiver as realized in the commercial-scale GEMASOLAR power plant near Seville, Spain (formerly Solar Tres) is based on the design used in the SOLAR TWO project: Thin vertical steel pipes are arranged like a cylinder on top of the tower and absorb the concentrated solar radiation on their outer surface. The molten salt is streaming on the inside of the tubes. This type of receiver is suitable for a surrounding heliostat field, which allows the receiver to be employed in large-scale power plants. A number of recent projects using molten salt are planned to include an open receiver. The disadvantage of this design is the direct exposure of hot surfaces to the ambient, to which almost all reflected and emitted radiation is lost. Since natural convection is not restrained by a surrounding structure and wind can directly impinge on the hot absorber tubes, convective losses are also high.

## I. Modeling and Simulation

The surface cavity receiver absorbs the solar thermal radiation. The heat is conducted along the cavity walls. When the fluid HTF passes through the tubular media, heat is transferred from walls to HTF. The flow and heat transfer can be simplified as described in Fig. 1.

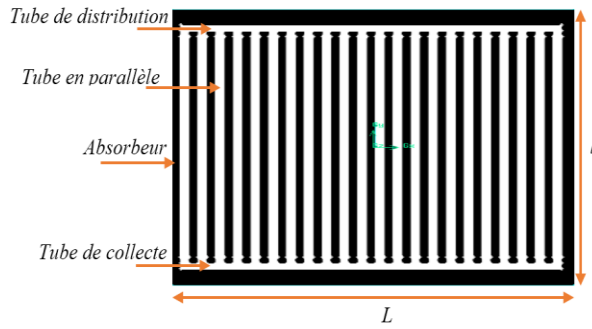


**Fig.1.** Schematics of the flow through a surface tubular solar receiver.

The calculating domain is defined by a cross section of the cavity solar receiver where the cavity is provided with a number of tubes connected in parallel as shown in Fig.1.

In order to construct the geometry describing the studied problem, we have to define the coordinates of some points that are used to create the considered configuration. For this, the commands used are the following: Create a real point at the specified coordinates, create a real segment from existing points, finally create a real face from existing segments. This study is developed to analyze the evolution of the velocity, temperature and pressure fields in the considered configuration depending on the aspect ratio defined as follows:

$$\Gamma = \frac{L}{l} \quad (1)$$

Where  $L$  is the cavity length and  $l$  is its width.

Towards the end, we can draw conclusions from the results in qualitative and quantitative terms.

## II. Geometry Meshing with Gambit

The mesh is defined by the subdividing of the flow domain to an infinitely small sub-domains whose shape and number are imposed by the nature of the treated case. In our case, the mesh is quadrilateral.

In order to solve the problem numerically, we have to establish an adequate meshing test performed through the test of numerous meshings in order to determine the appropriate number of nodes and to optimize the

time and storage space before the execution of any systematic calculation (Fig.I.2).

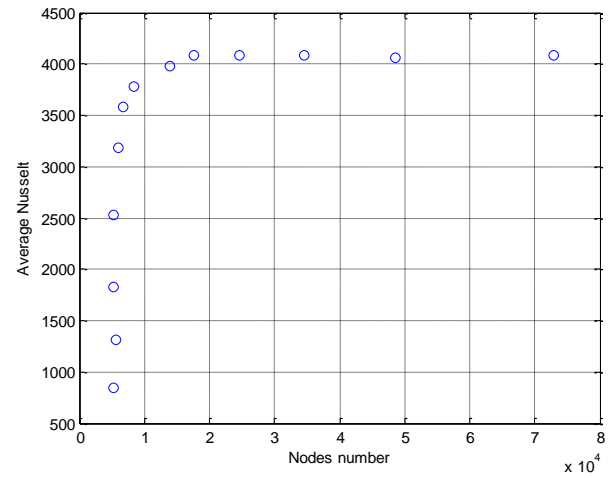


**Fig.2.** Schematics of meshing dependency, evolution of the average Nusselt number versus the nodes number.

Therefore, after testing, it was used a structured quadratical meshing compound of 20480cells, 41344 faces and 20865 nodes in the case of the system of  $L=2m$  and  $l= 1m$ .

### II.1. Boundary Conditions

In our case, we can define the border of the two areas: in tubular receivers where the tubes are in series and receivers where the tubes are in parallel which are defined by the geometric contours associated with the following elements:

- The walls of the absorber (cavity walls) of such **wall**.
- The fluid used in our study is the molten salt, it is the HTF **fluid**, characterized by a Prandtl number equal to  $Pr \in [0,004-15]$  with thermophysical properties assumed as constants.

Using melton salts as a heat transfer fluid HTF was tested by researchers at the Oak Ridge National Laboratory (ORNL National Laboratory): Williams and Williams et al.

They found that Molten salts seem to be very good candidates with some requirements. However, not the salt consists of a single component which obeys the requirement of a low melting point; but the salts having multiple components or mixtures

involve the performance of the latter condition.

### III. Solving with Fluent

Using Fluent's software allows us to build a numerical model capable of handling thermodynamics specificities linked to the process of heat transfer in the cavity of the solar receivers.

The main objective of this study, is to highlight the different effects influencing the process and the characterization of heat transfer in the cavity receiver where the tubes are linked in parallel.

For this, it is essential to mention the influence parameters acting on the process, the shape of the cavity (Effect of the Aspect ration or geometrical effect), the tube diameter, size of the cavity opening, the number of tubes, the mass flow rate, flow regime, external impacts as the heat flux, etc ...

## VI. Results and discussion

In this case of study, we treated only some effects such as the aspect ration effect, the inlet heat flux and the regime nature effect on the process of heat exchange in the cavity solar receiver.

### VI.1. Effect of Aspect Ratio

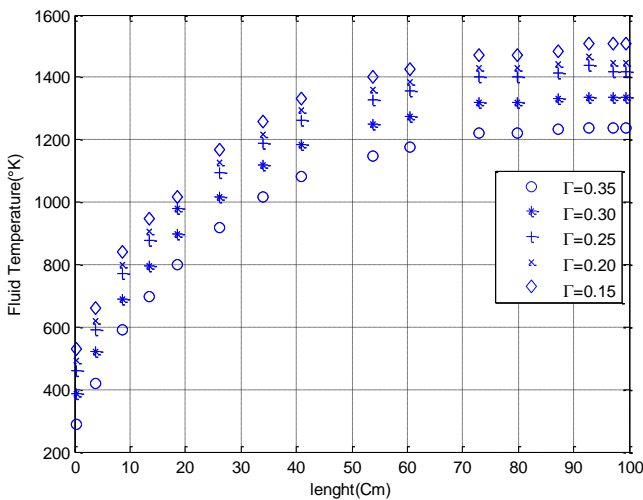


**Fig.3.** Influence of the aspect ration on the temperature distribution at  $q_w = 1MW / m^2$ .

The geometrical effect on the temperature distribution are shown in Fig. 3, in which the temperatures are plotted as functions of the aspect factor along the HTF flow direction. Five aspect ratio,  $\Gamma = 0.15, 0.20, 0.25, 0.30$  and  $0.35$ , are examined.

The fluid HTF temperatures are changed with increasing aspect ratio, the fluid temperature at the entrance is  $300 \text{ }^\circ\text{K}$  and at the outlet is between  $1200 \text{ }^\circ\text{K}$  and  $1500 \text{ }^\circ\text{K}$  for all values of  $\Gamma$ , but the temperatures of HTF flow decrease with increasing aspect ration.

The steady-state assumption forces the fluid flow temperatures to reach  $\sim 1500^\circ\text{K}$  at the outlet. Where, the thermal energy provided from the sun, is carried away by a convective heat transfer.

### VI.2. Effect of the inlet Heat flux

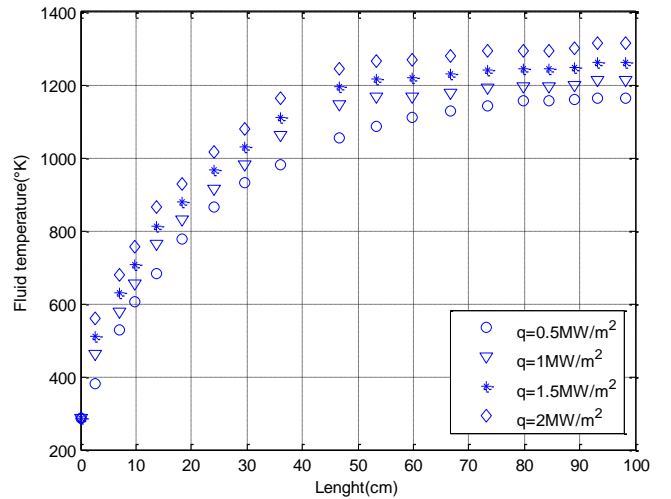


**Fig.4.** Influence of the inlet heat flux on the temperature distribution at  $\Gamma=0.25$ .

The previous figure shows the effect of the inlet heat flux on the temperature profiles. The variation in the inlet heat flux through the receiver wall depends on the field of heliostats, their number and their distribution around the solar tower, and depends also on the the solar time for a given day, month, year,...etc. Five heat flux, are examined in this study.

Along the HTF flow direction, the temperature of the receiver wall decreases slightly,

but the fluid temperature increases brusquely along this direction.

The receiver wall temperature increases also with increasing the inlet heat flux, the absolute value of solid temperature gradient is superior than the outlet one, which means that the diffusive flux have the major importance at the entrance region.

### VI.3. Effect of the Regime Nature

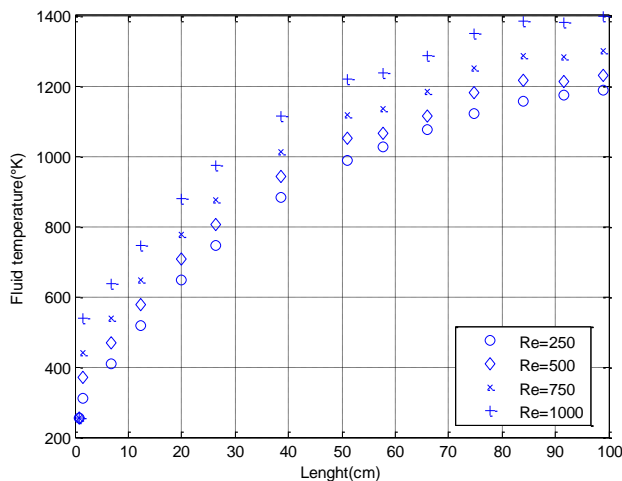


**Fig.5.** Influence of the regime nature on the temperature distribution at  $\Gamma=0.25$ .

By comparing the HTF temperatures profiles  $T_f=T(x,y)$  corresponding to the different Reynolds numbers ( different regimes), it is noted that heat transfer is more efficient for the higher values of Reynolds number. The isotherms are regular and intensified in the vicinity of the entrance region, while they are more intense in the middle the lower edge; they vary axially along  $x$  and remain constant along the exit region of the solar receiver .

It was found that the HTF temperature was strongly affected by the regime of forced convection and their maximum values increase as  $T_{max}$  as the Reynolds number increases.

### CONCLUSION

The results obtained from the numerical simulation using a suitable code "Fluent", based on the finite volume method to an op-

timized meshing has solved the governing equations of the heat transfer in the case of a cavity tubular solar receiver using a molten salts as a HTF(heat transfer fluid).

The analyzes of typical influences of the aspect ratio, the inlet heat flux and the regime nature on the temperature distributions lead us to focus on the shape of the cavity receiver in order to choose the optimal aspect ratio offering the maximum of heat exchange,

To find the sunniest Algerian site characterized by the most intense heat flux,

To pick the most rentable regime in terms of efficiency, thermal performance and energy losses.

### REFERENCES

Antonio L. Avila-Marin. Volumetric receivers in Solar Thermal Power Plants with Central Receiver System technology: A review. *Solar Energy* 85 (2011) 891–910. CIEMAT, Departamento de Energia, Avda. Complutense 22, E-28040 Madrid, Spain.

R. Chacartegui et al. Alternative cycles based on carbon dioxide for central receiver solar power plants. *Applied Thermal Engineering*. 31 (2011) 872e879. Thermal Power Group (GMTS), Escuela Técnica Superior de Ingenieros, Camino de los descubrimientos s/n, 41092 Sevilla, Spain.

Hennecke, K., Schwarzbozl et al. The Solar Power Tower Jülich: A Solar Thermal Power Plant For Test And Demonstration Of Air Receiver Technology. *Proceedings of ISES Solar World Congress 2007: Solar Energy and Human Settlement*.

Price H, Lüpfert E, Kearney D. Advances in parabolic trough solar power technology. *J Sol Energy Eng* 2002; 124(2):109–25.

Lei DQ, Wang ZF, Li J. The calculation and analysis of glass-to-metal sealing stress in solar absorber tube. *Renew Energy* 2010; 35(2):405–11.

Burkholder F, Kutscher, C. Heat loss testing of Solel's UVAC3 parabolic trough receiver. NREL/TP-550-42394; 2008.

Williams, D. F. 2006. Assessment of Candidate Molten Salt Coolants for the NGNP/NHI Heat-Transfer Loop, Oak Ridge National Laboratory Report ORNL/TM-2006/69.

Williams, D. F., Toth, L. M., and Clarno, K. T. (2006b). Assessment of Candidate Molten Salt Coolants for the Advanced High-Temperature Reactor (AHTR), ORNL/TM-2006/12, Oak Ridge National Laboratory, Oak Ridge, TN, March 2006.